Journal of Materials Chemistry A

ROYAL SOCIETY OF CHEMISTRY

REVIEW

View Article Online
View Journal | View Issue

Cite this: J. Mater. Chem. A, 2025, 13, 37700

Low-cost, large-area carbon electrode perovskite solar cells

Afsaneh Farokhi,[a] Hashem Shahroosvand, *[a] Fatemeh Naderloo,[a] Sebastiano Bellani,[b] Giulia Grancini, [c] Aldo Di Carlo, [de] Liberato Manna [f] and Mohammad Khaja Nazeeruddin *[gh]

The increasing efficiency of perovskite solar cells (PSCs), driven by their low cost, low carbon footprint and easy processability, offers real opportunities for new markets in innovative photovoltaic (PV) technology. A crucial challenge in this transition is device instability. Carbon-based perovskite solar cells offer a promising alternative with the advantages of more abundant materials and stable performance. This review provides a comprehensive and critical analysis of recent advancements in carbon-based PSCs (C-PSCs) technology, focusing on the applications of carbon electrodes and their critical role as interfacial electrodes, as well as discussing the advantage of this configuration in terms of deposition methods for large-area modules. Furthermore, techno-economic aspects will be considered to provide an assessment of the suitability of C-PSCs for applications ranging from large-area PVs to indoor applications and flexible electronics.

Received 23rd June 2025
Accepted 26th August 2025

DOI: 10.1039/d5ta05091j

rsc.li/materials-a

Introduction

Worldwide, electricity demand is growing faster than the energy supply.[1–3] In addition, the conversion of fossil fuels into electrical energy releases a large amount of CO_2 into the environment (11 Mt_{CO_2} per year),[4] posing increasing risks to health and the environment.[1,5–7] Therefore, there is an urgent need to shift from fossil fuel energy to clean, environmentally friendly renewable energy sources such as solar, geothermal, wave, wind, hydro, and hydrogen biomass.[1–3] Among these, solar energy stands out as the most abundant and accessible renewable resource.[1,2,8,9] Photovoltaics (PVs) present a particularly promising solution by directly converting sunlight into electricity without the need for intermediate steps. This simplified process improves efficiency and usability, allowing PV systems to produce significant amounts of electricity while maintaining a minimal environmental impact.[10,11]

The PV sector encompasses a diverse array of solar cell technologies, classified into distinct generations based on their materials and manufacturing processes.[12–15] In this context, the National Renewable Energy Laboratory (NREL) efficiency chart underscores the continuous improvement of power conversion efficiency (PCE) made across all generations of PV technologies.[16] First-generation solar cells are primarily based on silicon wafers and represent the most established and widely used technology in the PV industry, with a certified record PCE of 27.1%[16] and recognized longevity.[17,18] Second-generation solar cells utilize thin-film materials that are deposited on substrates, offering flexibility and lower manufacturing costs.[19] Key types include copper–indium–gallium–selenide (CIGS) solar cells with a record certified PCE of 23.3%.[16] Lastly, third-generation solar cells include advanced technologies that aim to surpass the performance limitations of first- and second-generation cells through innovative materials and structures.[20,21] Representative examples are perovskite solar cells (PSCs), which can achieve PCEs exceeding 26% in laboratory settings[22] (certified PCE as high as 26.7%)[16] while offering easy and cost-effective manufacturing.

Each generation of solar cells brings distinct advantages and challenges, contributing to the ongoing evolution of PV technology and its role in addressing global energy needs. As research progresses, advancements in these technologies continue to push the boundaries of efficiency, cost, and application potential, paving the way for more sustainable and widespread use of solar energy.

In this context, PSCs stand out as a next-generation technology that could revolutionize the PV industry, offering the potential for flexible, wearable, and highly efficient single-

[a]Group for Molecular Engineering of Advanced Functional Materials (GMA), Chemistry Department, University of Zanjan, Zanjan, Iran
[b]Antares Electrolysis S.r.l., Piazza della Vittoria 14/19, Genova, 16121, Italy
[c]Università Degli Studi Di Pavia - Pavia (Italy), Department of Chemistry & INSTM, Via T. Taramelli 14, 27100 Pavia, Italy
[d]ISM-CNR, Istituto di Struttura della Materia, Consiglio Nazionale delle Ricerche, Via del Fosso del Cavaliere 100, Roma, 00133, Italy
[e]CHOSE, Centre for Hybrid Organic Solar Energy, Department of Electronic Engineering, University of Rome, Tor Vergata, Via del Politecnico 1, Roma, 000133, Italy
[f]Nanochemistry Department, Istituto Italiano di Tecnologia, Genova 16163, Italy
[g]Group for Molecular Engineering of Functional Materials, Institute of Chemical Sciences and Engineering, École Polytechnique Fédérale de Lausanne, CH-1951 Sion, Switzerland. E-mail: mdkhaja.nazeeruddin@epfl.ch
[h]School of Integrated Circuits, Southeast University, Wuxi 214026, Jiangsu, P. R. China

junction solar devices that are easier and cheaper to manufacture compared to traditional silicon-based solar cells.[23,24] In addition, combining the PSC in tandem with silicon solar cells has reached over 34% power conversion efficiency.[25,26] This rapid improvement is driven by the exceptional optoelectronic characteristics of perovskite materials, which include high charge carrier mobilities of 0.1–10 $cm^2\ V^{-1}\ s^{-1}$, low trap densities, defect tolerance,[27–29] a tunable bandgap, and long charge diffusion lengths under open-circuit conditions.[24,29,30] Perovskite materials exhibit a versatile structural framework, encompassing configurations with different dimensionalities (3D, 2D, quasi-2D, 1D, and 0D).[28] The most commonly studied photoactive halide perovskites have a 3D crystal structure represented by the chemical formula ABX_3, where A is a monovalent cation such as methylammonium ($CH_3NH_3^+$, denoted as MA^+), formamidinium ($HC(NH_2)_2^+$, denoted as FA^+) or cesium (Cs^+), B is a divalent metal cation (typically Pb^{2+} or Sn^{2+}) and X is a halide anion (Cl^-, Br^- or I^-).[15,31,32] PSCs are available in two device architectures: the regular (n–i–p) structure and the inverted (p–i–n) structure. In these configurations, the perovskite material serves as the light-absorbing layer with intrinsic semiconductor properties, while the surrounding semiconductors act as charge-selective layers. The regular architecture can be further divided into mesoporous or planar types based on the morphology of the n-type charge-selective layer. In the mesoporous type, a porous scaffold is used to enhance charge extraction, while the planar type relies on a compact layer. These diverse configurations underscore the flexibility and potential of PSCs in advancing solar energy technologies.[33,34]

Carbon electrodes in PSCs

Carbon materials are highly suited for PV applications, offering exceptional electrical conductivity, chemical stability, and structural adaptability.[35–37] Moreover, their abundance, low production costs, and environmental friendliness position carbon as a sustainable and economical alternative to costly noble metals traditionally used as electrodes in solar cells.[35–37] Various carbon allotropes with different dimensionalities are particularly effective in enhancing the performance of PSCs. These include 0D nanoparticles (fullerene, C60), 1D linear structures (carbon nanotubes, CNTs), 2D nanosheets (graphene),[37,38] and 3D structures like activated carbon, carbon black, and graphite (Fig. 1a).[37] Owing to their multifunctional properties, carbon-based materials are utilized across various layers and interfaces within PSCs, contributing to enhanced efficiency, stability, and sustainability (Fig. 1b–e).[37,39–41] Among the different components of PSCs, the back (counter) electrode has been a focal point for innovation, particularly in replacing traditional metal electrodes, leading to the so-called carbon PSCs (C-PSCs).[42–44] This transition is crucial for advancing PSC technology toward more scalable and cost-effective production.[43,45,46] In particular, eliminating metal electrodes in PSC technology addresses issues of high cost, resource scarcity, and environmental impact while improving scalability and stability.[41,47] Traditional PSCs employ precious metals such as gold (Au) and silver (Ag) as rear electrode materials, but their deposition requires energy-intensive processes such as thermal evaporation in high-vacuum environments, which complicates large-scale production and cost reduction.[41,48] Furthermore, Au and Ag can degrade cell performance and lifespan due to migration into the perovskite layer and corrosion from moisture or halides. In contrast, carbon materials offer a simpler and more sustainable solution, facilitating large-area deposition through high-throughput (roll-to-roll) printing methods for perovskite solar module (PSM) manufacturing.

Carbon-based films are commonly designed to feature flexibility, enabling flexible cell formats on lightweight plastic substrates,[49] compatible with industrial roll-to-roll

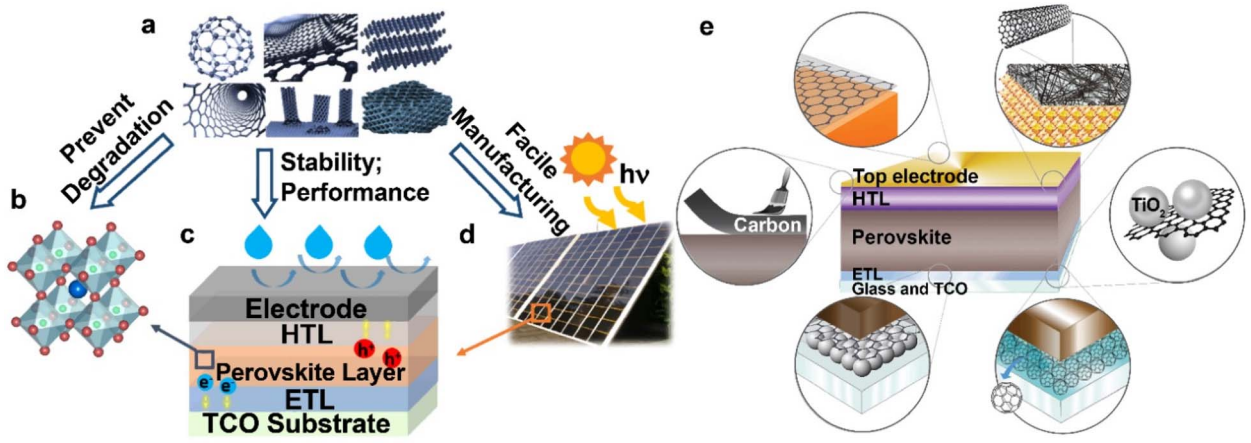

Fig. 1 Carbon-based materials in PSCs. (a) Various carbon allotropes, including fullerene, graphene, graphite, CNTs, and 3D structures, which have been utilized or hold potential for use in PSCs. (b) ABX_3 perovskite crystal structure, with blue, green, and red dots representing A, B, and X atoms, respectively. (c) Typical n–i–p-PSC architecture, designed to enhance resistance against moisture intrusion. (d) A large-area PSM. (e) Schematic illustration of the applications of carbon-based materials in different components of a PSC. The n–i–p device architecture comprises a transparent conductive oxide (TCO) on top of a glass substrate, an electron-transporting layer (ETL), a perovskite layer, a hole-transporting layer (HTL), and the top carbon electrode. Panels (a–d) reproduced from ref. 37, Wiley-VCH. Panel (e) adapted from ref. 39.

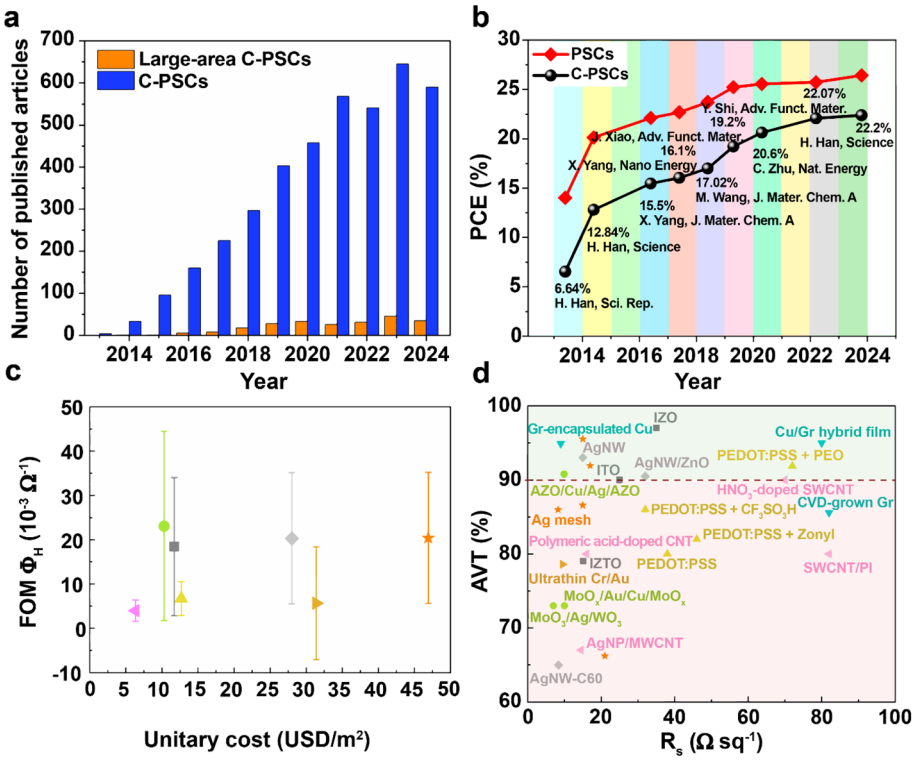

Fig. 2 Rapid advancements in C-PSCs. (a) Published article statistics from Web of Science, reflecting the growing research interest in the field. (b) Evolution of PCE values reported in the literature for PSCs and C-PSCs, demonstrating significant performance improvements over time. (c) Figure of merit (FOM) φ_M *vs.* unitary cost for various TCEs. The data underscore the trade-offs between performance and cost. (d) Comparison of TCEs based on R_s and average visible transmittance (AVT). The plot illustrates the performance landscape of different TCE materials, including AgNW, PEDOT:PSS, single-walled carbon nanotubes (SWCNTs), and graphene-based technologies, showcasing their potential for optoelectronic applications.

manufacturing.[50,51] In addition to flexibility, carbon electrodes also exhibit hydrophobicity, acting as protective barriers against moisture for long-term stable devices.[44,52,53] As shown in Fig. 2a, the growth in the number of publications related to carbon electrodes in PSCs reflects the increasing interest and research activity in this area. Significant progress has been made in enhancing the PCE of C-PSCs in recent years, as depicted in Fig. 2b.[54] The journey began in 2013 when Ku *et al.* first integrated carbon electrodes into PSCs, achieving a modest PCE of 6.64% using a carbon black/spheroidal graphite counter electrode in mesoscopic heterojunction PSCs.[55] Han *et al.* pioneered the development of fully printable PSCs with carbon electrodes, reaching a PCE of 12.8%.[56] Initially, the research focused primarily on devices without a HTL, which limited PCE improvements. However, in 2016, the introduction of n–i–p structures with various HTLs marked a turning point,[54] with Chen *et al.* pushing the PCE to 14.38%.[57] The following year, Jeon and colleagues advanced the C-PSCs by using CNTs as electrodes in a p–i–n architecture, leading to further improvements.[58] Zhang and colleagues subsequently increased the PCE to 15.9% in 2017.[59] Since then, substantial advancements have been achieved, with current C-PSCs now reaching PCEs as high as 22.2%, closely approaching those of metal-electrode-based PSCs.[60] This improvement is complemented by (1) exceptional operational stability of C-PSCs,[47,54] attributed to the hydrophobic nature of carbon materials, which effectively prevent moisture-induced degradation; and [37,43] (2) mechanical flexibility of carbon-based films,[37] making them compatible with high-throughput roll-to-roll manufacturing processes.[37,50]

In addition to carbon back electrodes, transparent carbon electrodes (TCEs) are often reported for PSCs as potential solutions to balance cost, stability, and performance, especially when compared to traditional TCOs and emerging alternatives such as silver nanowires (AgNWs) and conductive polymers.[61] The Haacke parameter (φ_M) is a metric used to evaluate the performance of transparent conductive materials, specifically their balance between optical transparency and electrical conductivity. It is calculated as follows:

$$\varphi_M = T^{10}/\sigma_{sh},$$

where T is the transmittance (typically measured at a specific wavelength, *e.g.*, 550 nm for visible light) and σ_{sh} is the sheet resistance of the material. Higher transparency and lower sheet resistance yield a higher ϕ_M value, making materials with superior optical and electrical properties more favorable. The exponent T^{10} heavily weights transparency, as achieving high optical transparency is typically more challenging than conductivity. Despite recent progress on TCEs, carbon materials typically have a lower transparency-to-conductivity ratio than

TCOs, meaning they often require structural modifications to achieve satisfactory performances. Thus far, TCOs, *e.g.*, indium tin oxide (ITO) and fluorine-doped tin oxide (FTO), remain the industry standard, with σ_{sh} values on the order of 1–10 Ω sq^{-1} and transparencies >85% (TCOs can reach φ_M values as low as $\sim 5 \times 10^{-2}/\Omega$).[62] The successful spray pyrolysis deposition of an effective TCO has eliminated the reliance on vacuum processes,[62] making it even more challenging to economically compete with them when flexibility is not a strict requirement. Traditional TCEs consist of conductive polymers, such as solution-processed poly(3,4-ethylenedioxythiophene) polystyrene sulfonate (PEDOT:PSS).[63] In this material, the hydrophobic and conducting PEDOT and the hydrophilic electrically insulating PSS are ionically bonded together, allowing the material to be dispersed in polar solvents. While PEDOT:PSS has been widely established as a hole transport material (HTM) thanks to its high transparency, excellent flexibility and thermal stability, its conductivity is limited by the insulating nature of the PSS component.[64] Post-treatment methods (*e.g.*, acid doping) enhance its conductivity, reducing sheet resistance to 30–50 Ω sq^{-1} with a transparency around 85%. This treatment allows PEDOT electrodes to achieve ϕ_M values that are competitive with those of TCOs, around $10 \times 10^{-2}/\Omega$.[65] Nevertheless, PEDOT has limitations in stability, especially under high humidity or thermal stress. Treatments with a strong acid, such as $HClO_4$, can lower σ_{sh}, but may damage plastic substrates such as polyethylene terephthalate (PET), limiting its application in flexible devices. Spray coating with mild acids has been effective, although it typically increases the manufacturing costs. Other TCEs made with materials such as graphene[66,67] or CNTs generally exhibit sheet resistances of around 100–300 Ω sq^{-1} with transparency values between 60 and 85% for visible light.[68,69] Their φ_M values are typically lower than those for traditional TCOs. However, recent innovations have introduced hierarchical carbon nanostructures as promising materials for TCEs, leading to PCEs of up to 14.1%.[70] Furthermore, their adaptability to low-temperature deposition processes allows them to be integrated into a broader range of substrates, including polymers, enabling their use in diverse applications such as wearable devices, portable electronics, and other semi-transparent PV systems. The ability of TCEs to withstand mechanical stresses without degradation further distinguishes them from TCOs, which are brittle and prone to cracking under flexural strain. These features position TCEs as a key enabler for the next generation of flexible and stretchable electronic devices. Future research is expected to focus on optimizing the synthesis processes of TCEs, enhancing their stability under environmental stressors, and reducing production costs to accelerate their commercial adoption. Additionally, combining carbon-based nanomaterials with other materials, such as AgNWs or conductive polymers, could create hybrid structures with tailored properties for specific applications, further expanding their utility. For example, AgNWs and metal grids, in combination with carbon-based materials, can reach 10–50 Ω sq^{-1} with >80% transparency.[71] These hybrids combine the flexibility and conductivity of metals with the stability and low cost of carbon but can suffer from high contact resistance and a tendency to oxidize. In addition, the high cost of AgNWs hinders their massive exploitation. Dielectric/Metal/Dielectric (DMD) structures have been proposed as another possible transparent electrode solution. However, while the metallic layer permits obtaining high electrical conductivity, its high reflectivity negatively affects *T*. Even though carbon materials can be relatively inexpensive, their large-area deposition in the form of thin films typically requires chemical vapour deposition (CVD) and film transfer processes, increasing the overall costs of TCEs. Solution-processed graphene alternatives, though less expensive, often fall short in electrical performance, thus constraining commercial adoption for semi-transparent PSCs. In conclusion, TCEs present a low-cost and flexible alternative to traditional TCOs, especially where flexibility and stability are prioritized over maximum conductivity and transparency. However, their φ_M values generally lag behind those of TCOs due to higher σ_{sh} values and moderate transparency levels. While hybrid structures involving AgNWs and graphene improve the performance, costs remain a barrier. Fig. 2c and d summarize the performance achieved by TCEs, categorized in different groups and compared to either TCOs or other emerging technologies.

Scaling up of C-PSCs

Despite their promising stability and efficiency, scaling C-PSCs from laboratory settings to large-scale production remains challenging.[72,73] Creating a pinhole-free and defect-free perovskite layer is essential for optimizing the performance and stability of large-area PSCs, regardless of the type of rear electrode used.[74,75] However, this becomes even more challenging with carbon electrodes due to the specific criticalities involved in their deposition process. Carbon electrodes are typically deposited from liquid viscous slurries (pastes), *e.g.*, by processes including doctor blade coating and screen printing. Other deposition processes are spray coating, spin coating, and inkjet printing, which, however, require low-viscosity carbon pastes, commonly referred to as inks.[46] Regardless of the viscosity of the pastes or inks, the solution-processing of carbon electrodes can inadvertently damage the perovskite or other functional layers. These processes can therefore increase the likelihood of short circuits, a problem that is less pronounced with the use of thin metallic electrodes, which generally allow for more controlled and uniform deposition. To mitigate issues associated with solvent leaching and the high-temperature processing needed for solvent removal, dry methods—categorized as pressing transfer or lamination techniques—have been proposed. However, achieving precise alignment of carbon patterns during the transfer process for carbon perovskite solar modules (C-PSMs) remains a critical challenge for industrial implementation, as discussed hereafter.

Perovskite deposition optimization

The inherently thicker and potentially less uniform carbon layers require careful process optimization to avoid compromising the integrity of the underlying perovskite layer, making

defect control in the latter even more critical compared to traditional cells based on metallic rear electrodes. In this scenario, research activities developed various strategies to obtain high-quality (uniform and dense) perovskite layers, including: (1) solvent engineering, considering anti-solvent quenching and solvent additives; (2) thermal annealing, *e.g.*, sequential annealing and hot-casting of perovskite precursors on a pre-heated substrate, as well as post-deposition annealing of the perovskite films; (3) compositional engineering, *e.g.*, the rational design of mixed cation and anion perovskites, the introduction of passivating agents (such as fullerene derivatives, alkylammonium salts, or polymers) into the perovskite precursor solution to passivate grain boundaries, and the use of polymer additives, such as polyethylene glycol (PEG) or polyvinylpyrrolidone (PVP), and inorganic additives, *e.g.*, alkali metals such as K^+ or Rb^+ salts, that enhance the crystallization and grain size needed for smooth perovskite films with reduced pinhole density; (4) optimizing deposition techniques and their parameters, screening large-area deposition methods beyond traditional spin coating, *i.e.*, blade coating and slot-die coating, and also vacuum-assisted deposition methods, mainly evaporation; (5) substrate engineering, including the substrate treatment with plasma or UV-ozone and the application of self-assembled monolayers (SAMs) that provide wettability towards perovskite precursor solutions; (6) layer-by-layer deposition, pursued to reduce the likelihood of pinhole formation. Scalable deposition techniques for large-area perovskite films have been reviewed in previous literature.[76]

Carbon electrode engineering and application methods

Beyond optimizing perovskite deposition methods, it is crucial to optimize the formulation of the carbon paste and its deposition to avoid the damage of the underling layers. To address these aspects, the main research areas include the following: (1) solvent engineering, considering the formulation of carbon paste with solvents that are chemically compatible with the device functional layers (*i.e.*, perovskite and charge-transporting layers, CTLs), while ensuring the rheological properties are suitable for the selected deposition technique; (2) carbon electrode processing, focusing on the screening of high-throughput large-area deposition techniques, including roll-to-roll printing ones (Fig. 3a),[50] while optimizing the deposition parameters to minimize chemical and thermomechanical stresses on the underlying layers during carbon electrode formation (*e.g.*, curing processes); (3) the development of dry transfer processes (Fig. 3b), also referred to as lamination processes, including hot-pressing,[77–79] cold-isostatic pressing (CIP)[80,81] and vacuum-aided laminations,[82,83] which avoid perovskite/CTL damage from organic solvents and scraping tools. However, these dry methods may complicate the upscaling of C-PSCs into C-PSMs because of stringent alignment requirements during the transfer of the carbon electrode atop the perovskite or CTL films;[77,79,80,84–86] and (4) the design of functional additives, *e.g.*, the incorporation of adhesion promoters that improve the adhesion of the carbon electrode to the perovskite or the CTL. Other additives may include pigments and materials that regulate the work function of the carbon electrodes, aiming to match it with the HTL valence band (for hole extraction in n–i–p PSCs) or the ETL conduction band (for electron extraction in p–i–n PSCs).[87–89] Fig. 4 illustrates the top PCEs achieved by large-area ($\geq$1 cm^2) C-PSCs made using various scalable deposition techniques for carbon electrodes.

Carbon electrode patterning

In the development of large-area perovskite-based PVs, the realization of minimodules, which are then connected into m^2-scale solar panels, is the most common approach towards commercially viable products.[90,91] Consequently, it is crucial to develop patterning techniques for the carbon electrodes.[92] In this context, the P1-P2-P3 patterning process is widely established to produce PSMs by interconnecting individual cells.[93–96] In more detail, this process involves three distinct laser scribing steps (P1, P2, and P3) that help define the active areas and electrical connections between the cells within a module.[93–96] The P1 scribing step is used to isolate individual cells within a module by creating grooves in the bottom conductive layer (typically a TCO like ITO or FTO). A laser is used to remove a narrow strip of the conductive layer along the desired scribe line. This step ensures that the cells are electrically isolated from each other. The P2 scribing step creates electrical interconnections between the layers, connecting the top of one cell to the bottom of the adjacent cell. A laser is used to remove the perovskite layer and the underlying CTL along a line that is slightly offset from the P1 scribe. This exposes the bottom electrode (previously patterned by P1) so that when the next layers (typically the last CTL and top electrode) are deposited, it contacts the bottom electrode of the adjacent cell. Lastly, the P3 scribing step is used to define the final cell areas and remove excess material from the top electrode (which is often a carbon or metal layer). A laser is used to scribe through the top electrode layer (and any intermediate layers) along a line that is offset from the P2 scribe but overlaps slightly with it. This removes the top electrode material from the edges of the cell, ensuring that the adjacent cells are electrically isolated. Laser patterning offers exceptional precision, allowing for highly accurate removal of the perovskite layer to create fine, well-defined scribe lines.[93,95,97] It is also well-suited for high-throughput manufacturing processes.[91]

It can be easily integrated into automated production lines, enabling rapid processing of large-area PSMs with consistent quality.[106] Notably, P3 can also be carried out by directly depositing patterned carbon electrodes, *e.g.*, by screen printing, or using mechanical scribing.[50,107,108] However, contrary to laser-based P3, these approaches are typically insufficient to minimize the inactive areas between cells, which directly reduces the overall PCE of the C-PSMs. Moreover, since screen printing and mechanical scribing are contact methods, the tools involved may experience physical wear and tear, which may damage the C-PSMs and lead to a higher scrap rate. While screen printing and mechanical scribing still have their roles, especially in specific contexts or for cost-sensitive applications, laser P3 patterning remains superior in terms of accuracy, throughput,

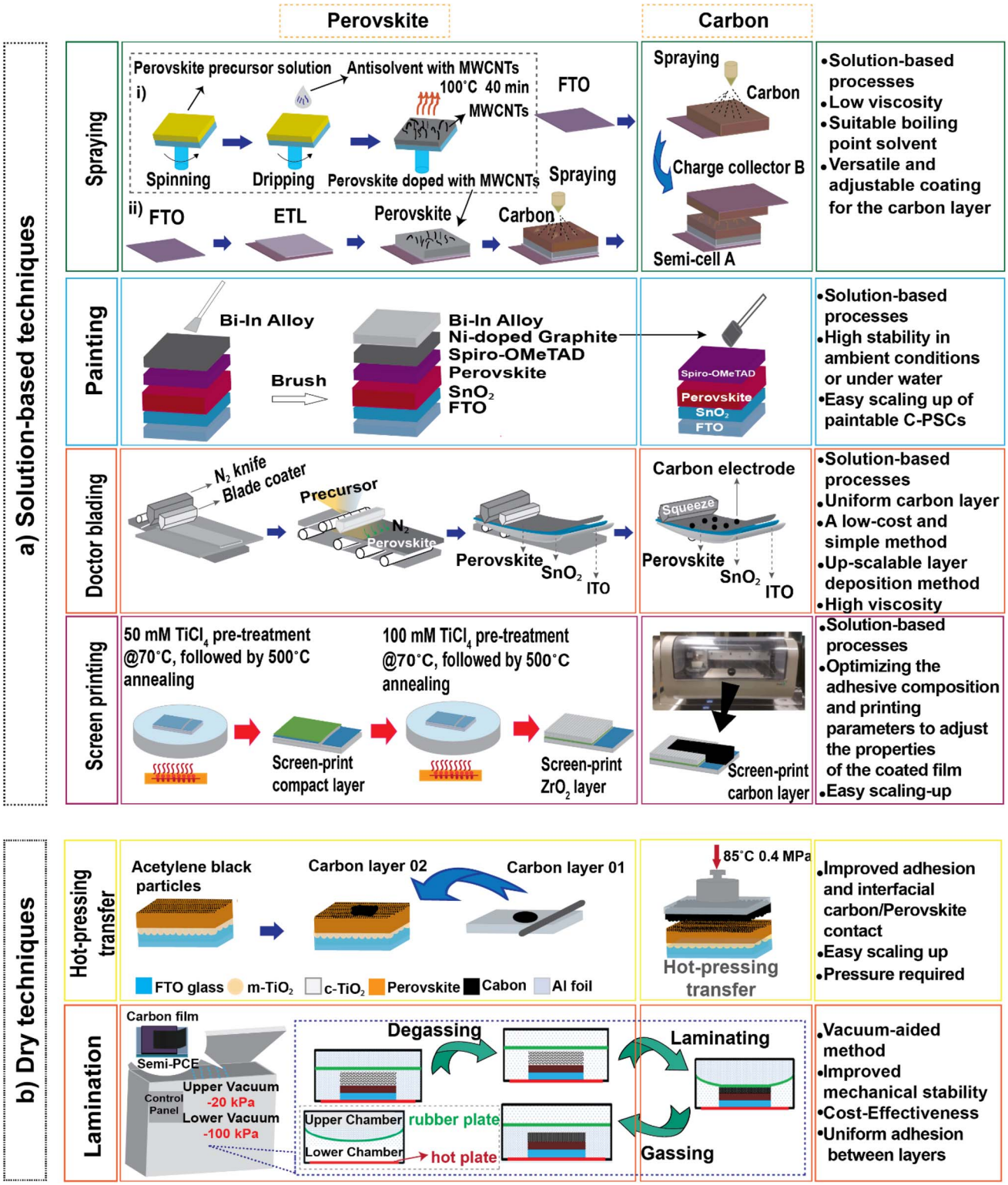

Fig. 3 Schematic illustration of the structure of large-area C-PSCs and their fabrication methods.

and the ability to maximize the active area of PSMs towards highly efficient large-area PSMs. However, the P3 process, though well-established for metallic rear electrodes, remains less understood and challenging when applied to thick (*e.g.*, 10–100 μm) carbon electrodes.[92] In particular, standard laser settings optimized for metallic electrodes may not be suitable for carbon, requiring careful adjustment of laser parameters (such as wavelength, pulse duration, and power) to achieve a clean cut without causing damage to the adjacent layers.[92] The risk of creating a short circuit due to incomplete scribing or

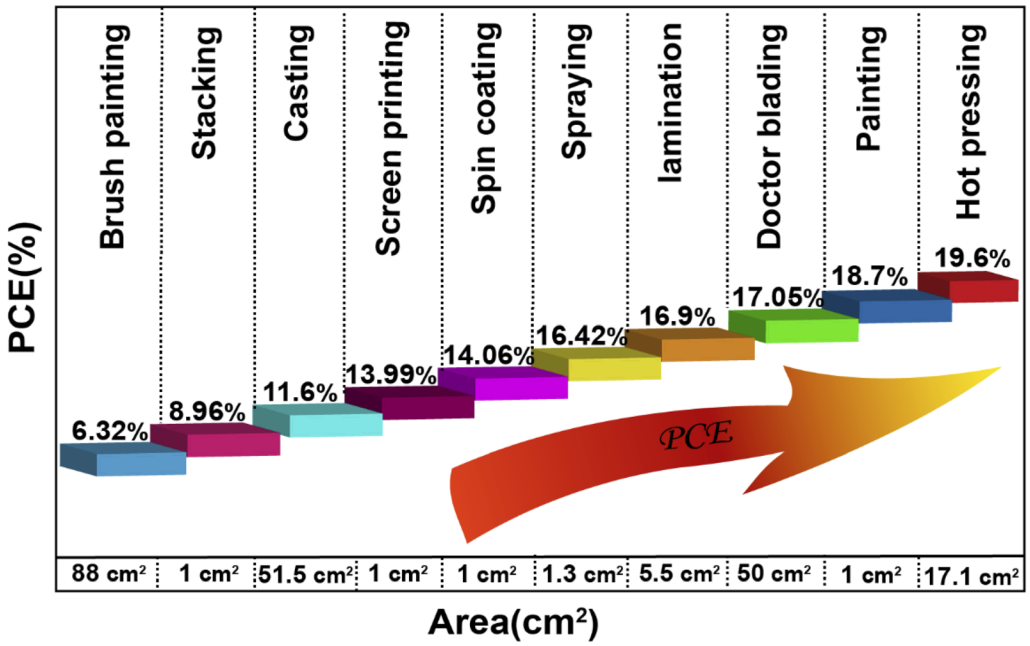

Fig. 4 Top PCEs measured for large-area (≥1 cm^2) C-PSCs using various scalable deposition methods for carbon electrodes.[42,80,98–105]

material residues left after patterning is higher with carbon electrodes. Laser patterning generates heat, which can be excessive when patterning too thick carbon electrodes. The heat generated during the laser process must be carefully controlled to avoid damaging the perovskite layer underneath or altering the properties of carbon electrodes, which may crack or delaminate under thermomechanical stress. Lastly, the surface roughness of carbon electrodes can interfere with the patterning process. A rough surface can cause scattering of the laser beam, leading to irregular cuts and making it difficult to achieve the desired precision. This irregularity can result in poor electrical isolation between cells, reducing the overall efficiency of the module. Overall, while P3 patterning is essential for creating efficient and reliable PSMs, the unique properties of carbon electrodes introduce challenges that must be addressed to advance C-PSM fabrication.

Notably, carbon electrodes may also be explored for the realization of wafer-like area PSCs,[42] as established in the Si solar cell industry, without relying on minimodule fabrication. Specifically, large-area, wafer-like solar cells reduce the need for interconnections between smaller sub-cells, which are necessary in minimodules.[109] This simplification potentially leads to a more streamlined manufacturing process with fewer steps and lower potential for manufacturing defects at the cell boundaries. Large-area cells have fewer edge boundaries compared to a collection of minimodules, minimizing edge losses and parasitic effects.[110] With fewer interconnections, large-area cells are less prone to failures that might occur at the connection points between minimodules.[111] This can enhance the long-term reliability and durability of the solar modules. Large-area cells also simplify solar panel assembly, avoiding the intricate steps required to connect multiple minimodules into larger arrays.[112] This can lead to lower production costs and improved yields. Large-area cells provide a more seamless and uniform appearance, which is particularly advantageous for building-integrated photovoltaics (BIPV) and other applications where aesthetics are important.[113] This seamless design integrates easily into architectural elements, avoiding visible seams or gaps. While large-area PSCs offer significant advantages over minimodules, their development faces several formidable challenges.[112] Key issues include the metallization of front electrodes made from TCOs and achieving uniformity in large-area perovskite layers. Although the research on large-area perovskite films is well-established, metallizing TCO layers in PSCs and other thin-film solar cells remains relatively unexplored. The challenge lies in the fact that the thickness of metallic fingers and busbars can disrupt the delicate thin-film structure, potentially affecting the cell's performance. To address these issues, techniques such as buried contact technology, embedding metallic contacts within the TCO or other layers, offer promising solutions but require further development. In contrast to the challenges associated with metallizing TCO layers, metallizing carbon electrodes is more manageable. This is largely because carbon electrodes can be effectively metallized using low-temperature metallic pastes. Commercially available pastes can be processed at temperatures below 120 °C, ensuring compatibility with the underlying layers and avoiding potential thermal degradation. Additionally, low-temperature metallic pastes are chemically compatible with carbon electrodes, reducing the risk of adverse reactions that could impact device performance.

Large-area demonstrators: C-PSMs

Until now, lab-scale C-PSCs with active sizes of around 0.05–1.0 cm^2 have achieved PCE values close to 20%, approaching those

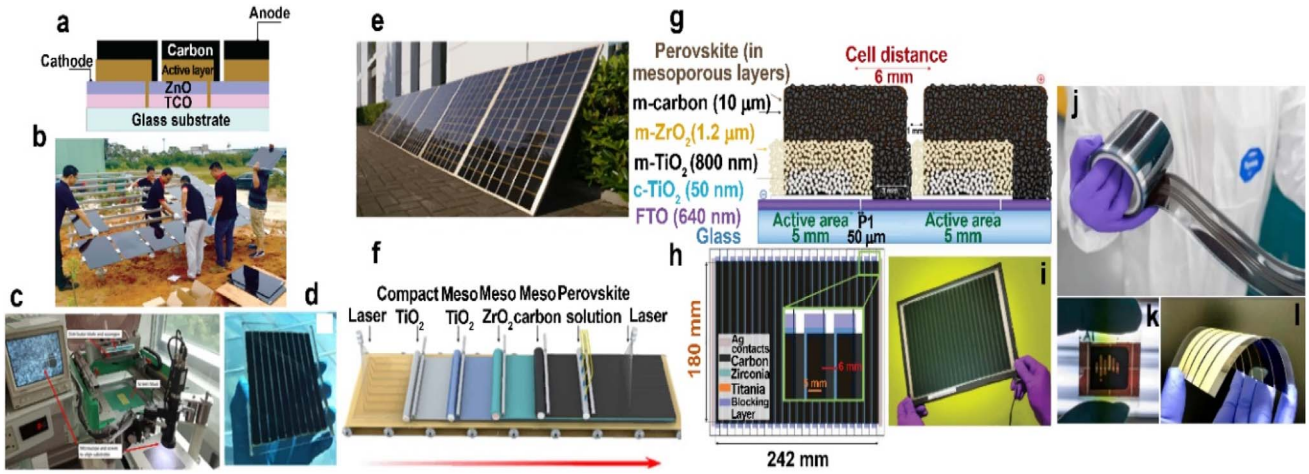

Fig. 5 Perovskite solar modules: (a) Architecture of the C-PSCs used to produce PSMs. (b) PSM installation into a solar farm. Panels (a and b) reprinted with permission from ref. 114, IOP Publishing. Fabrication of large-scale meso C-PSCs: (c) Photograph of a semi-automatic screen printer. (d) Mesoscopic C-PSMs prepared by screen printing. (e) 7 m^2 solar panels made of mesoscopic C-PSMs. (f) Schematic illustration of the proposed production line of mesoscopic C-PSMs. Panels (c–f) adapted with permission from ref. 72, Cambridge University Press. PSMs: (g) Cross-section schematics of adjacent cells in the module with a nominal thickness of each layer, highlighting the laser-etched FTO, patterning of the TiO_2 blocking layer, and the electrical vertical connection enabled by the carbon back contact. (h) Module schematics showing the different overlapping layers, the dimensions of the active area for both the individual single cell and the whole module, as well as the distance between adjacent cells (inset). (i) Photo of a module; wires soldered to Ag-painted busbars provide robust electrical contacts. Panels (g–i) adapted with permission from ref. 117, Wiley-VCH. Flexible PSCs: (j) A sample of the fully roll-to-roll-printed C-PSCs. Credit: Swansea University (from Techxplore). (k) The back side of a C-PSC with a custom-designed electrode after CIP processing. Image credit: *Communications Materials*. (l) Photo: Hasitha Weerasinghe/CSIRO PSM. Panels (j–l) adapted with permission from ref. 118.

of metal-electrode-based PSCs.[47] Large-area C-PSMs are mainly reported using "minimodule" formats, focusing on active areas of at least 10 cm^2.[47] By optimization of the C-PSC architecture (Fig. 5a), Cai *et al.*[114] successfully attained a PCE of 10.6% in a C-PSM with an active area of 17.6 cm^2. Additionally, they scaled up efforts to develop larger modules measuring 45 × 65 cm^2, and constructed a solar farm featuring 32 perovskite panels (Fig. 5b).[47] Mesoscopic C-PSCs were manufactured using screen-printing techniques on rigid glass substrates, achieving a PCE greater than 10% for PSMs with active areas of 70 and 49 cm^2 (Fig. 5c and d).[115,116] Hu *et al.* significantly advanced the field by scaling up and integrating into a module size of 7 m^2, enabling integration into solar farms. Additionally, they have outlined a production line, as depicted in Fig. 5e.[115] In 2018, De Rossi and colleagues made a significant breakthrough in scaling up C-PSCs by demonstrating the largest C-PSM to date, with an active area of 198 cm^2 (ref. 117) (Fig. 5g–i). A group of researchers at Swansea University have developed fully roll-to-roll printed C-PSCs by utilizing a mix of low-temperature device design and roll-to-roll-compatible solution-processable electrodes, overcoming interlayer incompatibilities and recombination losses. The team developed a carbon ink compatible with both the device's underlying layers and the rheological requirements of roll-to-roll slot-die coating (Fig. 5j), achieving a stabilized PCE of 10.84%, comparable to previous roll-to-roll-coated devices with evaporated metal contacts.[118] Meanwhile, scientists from Monash University in Australia and CSIRO Manufacturing have reported a method called CIP to produce a flexible PSC with a bilayer electrode composed of carbon and Ag. This electrode rivaled Au-carbon electrodes in terms of PCE and stability, while offering a cost-effective solution (Fig. 5k).[118] Afterwards, the same research teams developed flexible PSMs using a roll-to-roll printing process, demonstrating significant potential for mass production. The so-produced cells achieved a PCE of 16.7% after the initial fabrication of an electrode from carbon and Ag on a detachable PET substrate, which was then pressed onto the PSC. The PET layer was subsequently removed and reused (Fig. 5l).[118]

Flexible C-PSCs (FC-PSCs)

FC-PSCs have garnered significant interest compared to their rigid counterparts due to their lightweight properties and mechanical flexibility. Achieving strong interface contact between the CTL and the carbon electrode is often challenging, which results in somewhat lower PCEs than those of rigid devices. Nevertheless, ongoing research has shown promising developments in FC-PSCs (Fig. 6 and 7). Flexible substrates for large-area C-PSCs are generally classified into two categories: polymer substrates (*e.g.*, polyethylene naphthalate (PEN) or PET) and metal substrates (*e.g.*, stainless steel, titanium, and copper foils).[119] In one study, optimizing the anodization time for the formation of compact TiO_2 and using a tri-layer graphene/polydimethylsiloxane (PDMS) electrode with a flexible titanium substrate led to a PCE of 15.0% (mask area = 1 cm^2) when laminated with polytriarylamine (PTAA) as the HTL. The device exhibited excellent bending stability, retaining performance after 1000 bending cycles at bending radii of 12 mm, 8 mm, and 4 mm (Fig. 6).[120] In FC-PSCs with regular (n–i–p) or inverted (p–i–n) configurations, PEN/ITO or PET/indium zinc

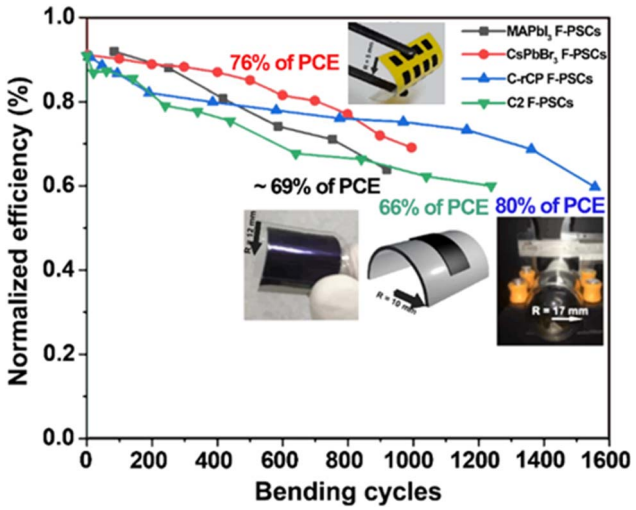

Fig. 6 Bending test of FC-PSCs.

oxide (IZO) substrates can be employed. Most FC-PSCs follow a regular structure, with TiO_2 or SnO_2 serving as the ETL. Scalable production of efficient, low-cost C-PSCs, using ambient low-temperature processes, has led to the development of $CsPbBr_3$-based devices.[121] For example, spray-coating CsBr onto spin-coated $PbBr_2$ films followed by thermal annealing resulted in a preferred crystal orientation (evolving from [020] into [031]). An all-inorganic $CsPbBr_3$-based FC-PSC achieved a PCE of 8.27%, slightly higher than its rigid counterpart (8%).[121] After 1000 bending cycles with a bending radius of 5 mm, the flexible device retained 76% of its initial PCE, demonstrating excellent flexibility (Fig. 6).[121] Self-adhesive carbon film electrodes, applied *via* the pressing transfer method, have shown the potential for higher PCEs than those of devices based on Au electrodes.

Highly efficient and mechanically robust flexible PSCs were fabricated using an ultra-simple all-carbon electrode configuration. The device structure was PEN/carbon/SnO_2/perovskite/C, where the top carbon electrode consisted of CNTs combined with a low-concentration graphene layer. Large-area devices with an active area of 1.0 cm^2 achieved a PCE of 10.38%, confirming both the electrode design and its suitable optical transmittance, excellent flexibility, and enhanced conductivity. After 4000 bending cycles with a bending radius of 4 mm, the hot-pressed flexible device retained ~71% of its initial PCE, demonstrating the strong mechanical flexibility of the all-carbon-electrode FC-PSC.[122]

A modified room-temperature ethanol solvent process was used to prepare reduced graphene oxide (rGO)-carbon quantum dots (CQDs)-PEG composites as carbon electrodes (C-rCP). Rigid C-rCP devices achieved higher PCEs (12.70%) than their flexible counterparts (8.80%) when employing mixed cation perovskites and spiro-OMeTAD. After 1000 bending cycles at a bending radius of 17 mm, the flexible devices retained 80% of their initial PCE (Fig. 6).[123] Further improvements were achieved with triple-cation perovskites and SnO_2/[6,6]-phenyl-C61-butyric acid methyl ester (PCBM) layers, leading to a PCE of 14.05% using carbon/conductive cloth as the back electrode, applied through pressing transfer. The conductive cloth's flexibility and softness enabled high performance in both rigid and flexible devices. Notably, a device based on a self-adhesive carbon/conductive cloth electrode exhibited excellent bending stability, with a PCE degrading to 66% of its initial value after 1240 bending cycles at a 10 mm bending radius (Fig. 6).[124] For FC-PSCs, the highest PCE of 15.18% was reported in the p–i–n configuration, namely, PET/IZO/PTAA/$Cs_{0.04}(FA_{0.83}MA_{0.17})_{0.96}$-$Pb(I_{0.83}Br_{0.17})_3$/PCBM:polymethylmethacrylate (PMMA)/Cr/C. The inclusion of an ultrathin Cr buffer layer facilitated ohmic contact and effective electron collection. These FC-PSCs also

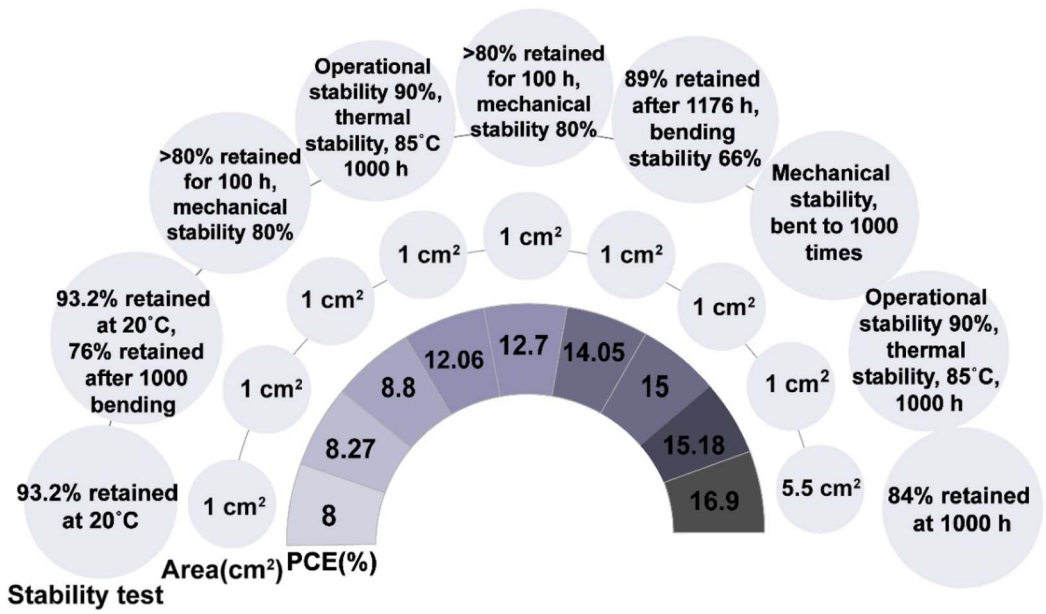

Fig. 7 Stability achievements for large area (≥1 cm^2) rigid C-PSCs and FC-PSCs.

exhibited exceptional operational stability at the maximum power point (MPP) and thermal stability (85 °C) for over 1000 h.[125] A high-pressure fabrication technique for rigid and FC-PSCs achieved a PCE of 16.9% for a 5.5 cm^2 cell, retaining over 84% efficiency after more than 1000 h.[80] Highly efficient and reliable super-flexible perovskite solar cells were successfully showcased on PEN substrates using graphene as a transparent electrode. The device achieved a performance of 16.8% without hysteresis, similar to that of the counterpart made on a flexible indium-tin-oxide electrode, which exhibited a maximum efficiency of 17.3%. The flexible devices also exhibited excellent stability against bending deformation, retaining over 90% of their original efficiency after 1000 bending cycles, and 85% even after 5000 bending cycles with a bending radius of 2 mm.[126] The mechanical characteristics, particularly the formation of cracks, in polycrystalline perovskite thin films were examined by altering the substrate thickness and identifying the fracture point. Understanding the fracture point led to the creation of a crack-free perovskite thin film on an extremely thin substrate (~2.5 μm). High-efficiency ultra-flexible perovskite photovoltaic devices (with a PCE of 17.03%) were fabricated. These devices preserved their performance after 10 000 bending cycles at a bending radius of 0.5 mm, which is a phenomenal result. Moreover, utilizing a hybrid transparent electrode made of a conducting polymer (PEDOT:PSS) and gold mesh grid, we effectively increased the active area (1.2 cm^2), achieving an efficiency of 13.6% for an area of 1 cm^2.[127]

The degradation rates of $MAPbI_3$ films induced by light have been investigated based on the charge polarity selectivity of the underlying transporting layer under various surrounding ambient conditions. Localized carrier polarities in the $MAPbI_3$ film were confirmed, as the charge selectivity of the underlying layer plays a crucial role in determining the degradation rate of the $MAPbI_3$ films. The $MAPbI_3$ films containing localized holes degraded more rapidly in the presence of H_2O compared to those with localized electrons, while an inverted trend of the degradation rate emerged under O_2-only ambient conditions. Notably, the mixture of H_2O and O_2 led to the fastest degradation for the localized hole-rich $MAPbI_3$ film, whereas the $MAPbI_3$ film with localized electrons was surprisingly stabilized compared to the O_2^--only condition.[128]

Despite the general understanding that ion instability mainly contributes to degradation, there is no observation of structural transformation at the atomistic scale. This observation is essential to understand how instabilities are induced by external perturbations such as illumination or electrical bias, enabling researchers to create effective methods to mitigate them. An *in situ* transmission electron microscopy setup was designed to facilitate real-time observation of amorphization in perovskite materials under electrical biasing. To reverse the device performance degradation caused by these structural changes, the samples were heated at 50 °C, which resulted in recrystallization and effectively restored their performance losses.[129]

C-PSCs based on 3D/2D and 2D/3D perovskites

The incorporation of a 2D perovskite into a 3D perovskite scaffold has recently gained significant interest as an innovative strategy to improve the stability of PSCs.[130,131] Large-area electrode-based PSCs using 3D/2D or 2D/3D perovskite configurations have been often studied as HTL-free designs. In these devices, a 2D perovskite (PEA_2PbI_4) and a 3D perovskite (triple cation CsMAFA) are used. The absence of an HTL allows the conduction and valence bands of the 2D perovskite interlayer to effectively mitigate interfacial charge recombination effectively. A post-treatment method was applied, where phenylethylammonium iodide (PEAI) reacted with excess PbI_2 in the pre-deposited perovskite layer, leading to the growth of the 2D perovskite (PEA_2PbI_4) at the interface between the 3D perovskite and carbon layers. This method resulted in a PCE of 10.05% achieved using screen-printed carbon electrodes. Suppressed ion migration contributed to the device's thermal stability, with no observed PCE loss after heating to 150°C.[132] By spin-coating a PEAI solution on a pre-deposited 3D perovskite and tuning the composition of the perovskites, a PCE of 11.76% was obtained for low-temperature-processed C-PSCs, attributed to the reduced defect density and diminished non-radiative recombination.[133] In addition, 3D/2D C-PSCs benefit from anchoring 2D perovskites such as the $(HOOC(CH_2)_2NH_3)_2PbI_4$ perovskite at the mesoporous oxide lattice, where they serve as both a protective barrier and a template for the growth of a stable 3D $CH_3NH_3PbI_3$ perovskite. This results in an orthorhombic phase that remains stable at room temperature. This molecular junction between 2D/3D perovskite structures has achieved a PCE of 11.9%. Additionally, an ultra-stable, fully printable large-area (10 × 10 cm^2) module C-PSM reached an 11.2% PCE with long-term stability exceeding 5000 h.[134] Another promising approach for enhancing PSC stability and efficiency is the use of 1D perovskite materials as stabilizers, which shield the 3D perovskite due to their excellent carrier transport properties and structural flexibility. These materials effectively passivate defects, and the production of $TFPbI_3$ facilitates perpendicular crystal growth. As a result, micromodules with an aperture area of 11.8 cm^2, based on a 1D@3D perovskite structure, demonstrated resilience under moisture and thermal stress, achieving a PCE of 12.48%.[135] Recently, Mallick *et al.* reported improvements in perovskite solution infiltration by converting 2D PEA_2PbI_4 perovskites into 3D $FAPbI_3$ and $FA_xMA_{(1-x)}PbI_yBr_{(3-y)}$ perovskites, overcoming the challenge of poor infiltration. Compared to $FAPbI_3$, the mixed-cation perovskites showed better stability due to the incorporation of FA and Br during the cation exchange process. The minimodule, fabricated by connecting two cells with a 2 cm^2 (0.5 cm × 4 cm) active area, achieved a PCE of 6.30%.[136] The PCE was further increased to 7.69% for a 1.2 cm^2 active area, due to an isopropyl alcohol (IPA) solvent vapor annealing treatment that enhanced perovskite crystallinity, improved pore filling, and produced a more homogeneous perovskite film morphology when using the 2D/3D mixed $(5\text{-AVA})_x(MA)_{1-x}PbI_3$ perovskite precursor

solution.[137] Nazeeruddin and colleagues created an ultra-stable 2D/3D $(HOOC(CH_2)_4NH_3)_2PbI_4/CH_3NH_3PbI_3$ perovskite junction, resulting in a C-PSC with one-year stability. Afterwards, C-PSMs were produced using 8 cells, each measuring 85 × 7 mm^2, resulting in an active area of 5.95 cm^2 per cell and 47.60 cm^2 per module. To demonstrate the scalability of the technology, fully printed industrial processes were employed to fabricate 10 × 10 cm^2 C-PSMs. These modules maintained a PCE of 11.2% over >10 000 h, with no performance loss under controlled standard conditions.[53] By incorporating long-chain 2D $C_6H1_8N_2O_2PbI_4$ ($EDBEPbI_4$) (EDBE = 2,2-(ethylenedioxy)bis(ethylammonium)) microcrystals into a 3D perovskite precursor solution, the grain boundaries of the 3D perovskite film were vertically passivated with a phase-pure 2D perovskite. This vertical alignment does not impede charge-carrier extraction from the 3D perovskite to the electrodes. The 2D/3D blend significantly improved the grain size, carrier lifetime, and vertical diffusion lengths. The C-PSM, consisting of six cells, each with an area of almost 10 × 10 cm^2 (active area 57 cm^2), resulted in an active area of 342 cm^2 per module. Using a $FTO/SnO_2/m\text{-}TiO_2/(EDBEPbI_4)_{0.03}[Cs_{0.05}(FA_{0.83}MA_{0.17})_{0.95}Pb(I_{0.83}Br_{0.17})_3]_{0.97}$/Spiro-OMeTAD/C configuration, these C-PSMs achieved a PCE of approximately 11.59%.[138] Building on the 2D/3D perovskite concept, a polymer was developed through the self-polymerization of ethylene dimethacrylate (EDMA) and polyhedral oligomeric silsesquioxane (POSS). This polymer layer, processed from a solution that does not degrade the 3D perovskite, effectively limits ion diffusion. An impressive PCE of 19.6% was recorded for minimodules with a carbon cathode, featuring an aperture area of 17.1 cm^2. This was achieved through a novel 3D/2D perovskite modification with a certified stabilized PCE of 18.2%.[105] This breakthrough opens new possibilities for fabricating C-PSCs based on 2D/3D perovskites, bringing them closer to commercialization.

Composite carbon electrodes for C-PSCs

Carbon black, CNTs, and graphene are the electrically conductive carbonaceous pigments most commonly used for the formulation of carbon pastes for C-PSCs. Carbon black is a cost-effective material commonly used to fabricate C-PSCs with satisfactory PCE values, as well as ambient stability even without any encapsulation.[139] Bio-carbons, produced from recycled waste materials through carbonization processes, are also being explored as low-cost and environmentally friendly carbon pigments. These materials offer well-aligned band structures and superior capabilities for extracting and collecting photo-generated holes.[140] However, due to the intrinsically weak contact at the perovskite/carbon (C) interface, the initial PCE of biomass-derived carbon electrodes remains suboptimal. Recent advancements have improved PCEs from 10.19% to a certified value of 11.08% by utilizing N,O co-doped porous composite carbon electrodes. These were created by mixing pyrolyzed dicyandiamide (DICY), KOH-activated soybean dregs, conductive carbon black (CCB), and PMMA for an $FTO/c\text{-}TiO_2/m\text{-}TiO_2/CH_3NH_3PbI_3$/N-KSDC/C structure.[141] A PCE of 6.32% was achieved for an 88 cm^2 all-solution-processed single-cell C-PSC. This improvement resulted from a layer-by-layer approach using bio-inspired graphitic carbon, extracted from an invasive plant species, and a mixed halide perovskite ($CH_3NH_3PbI_{3-x}Cl_x$). This interface-engineered structure ($FTO/c\text{-}TiO_2/m\text{-}TiO_2/CH_3NH_3PbI_{3-x}Clx/GC@CH_3NH_3PbI_{3-x}Cl_x/C$) further improved device stability and performance.[98] Since the perovskite/C interface is effective in accelerating hole transport between the two layers, multi-walled carbon nanotubes (MWCNTs) have emerged as promising carbon electrode materials. MWCNTs exhibit a satisfactory work function, superior film formation ability, high conductivity, and an advantageous tubular morphology, which ensures better interface contact compared to graphene and carbon nanocoils (CNCs).[142]

In the context of optimizing band alignment, embedding a sub-monolayer of nickel oxide nanoparticles (NiO NPs) before spraying MWCNTs improved the PCE from 8.99% in the $FTO/SnO_2/Cs_{0.05}(MA_{0.15}FA_{0.85})_{0.95}Pb(I_{0.85}Br_{0.15})_3$ structure to 10.33%. Finally, the PCE increased further to 11.2% when modular HTL-free large-active-area devices were employed.[143] To achieve optimized electrode structures and enhance conductivity, the doctor blade coating technique was used to fabricate NiO@CSs (carbon spheres)-composite electrodes *via* a low-temperature process. This involved incorporating NiO into CSs (NiO@CSs-composites) in the $FTO/c\text{-}TiO_2/CH_3NH_3PbI_2Cl/NiO@CSs$ structure. Two variations, NiO@CSs and NiO-C&C, were tested, and PV characteristics indicated an increase in PCE from 11.7% to 12.5%, largely due to the presence of CS layers.[144,145] The benefits of graphene are also noteworthy. The application of a 2D honeycomb structure of graphene enhances electron mobility in PV devices, yielding a PCE of 8.96% for a 1 cm^2 active area, using graphene oxide's simple self-assembly method.[99] By depositing a low-temperature-processed graphene-based carbon paste atop prototypical large-area (1 cm^2) mesoscopic and planar n–i–p structures ($FTO/c,m\text{-}TiO_2$ or $SnO_2/Cs_{0.05}(FA_{0.85}MA_{0.15})_{0.95}Pb(I_{0.85}Br_{0.15})_3$/spiro-OMeTAD/C), PCEs of 13.85% and 14.06% were achieved, respectively. To demonstrate metallization compatibility with C-PSCs, the substrate area was expanded to 6.76 cm^2, and the aperture area to 4.00 cm^2, resulting in a PCE of 13.86%.[42] As carbon electrodes can be utilized in a diverse range of applications, a high-performance PSC based on a $CsPbI_3$ absorber layer and a fully printable three-layer carbon electrode was recently fabricated with the structure of $FTO/c\text{-}TiO_2/CsPbI_3$/spiro-OMeTAD/C. The carbon layers were comprised of a macroporous carbon layer at the bottom, a graphite layer in the middle due to its high conductivity, and a thin, dense layer on the top. The three-layer carbon electrode was applied to 1.0 cm^2 $CsPbI_3$-based perovskite solar cells and demonstrated a PCE of 18.14%, highlighting the potential of multilayer carbon electrodes to be cost-effective, show stable device fabrication, and demonstrate enhanced performance.[146] Notably, the sheet resistance and thickness of the carbon electrodes were significantly reduced by using carbon-coated FTO glass under pressure. Modular graphene-based PSCs (G-PSCs) with a large active area of 1.30 cm^2 achieved a PCE of 16.42%.[102] To mitigate voltage loss in HTL-free C-

PSCs, an ultrathin ferroelectric perovskite oxide $PbTiO_3$ layer was strategically inserted between $MAPbI_3$ and m-TiO_2, resulting in an impressive PCE of 12.08%.[147] Among the highest reported PCEs for this category of C-PSCs, a PCE value of 18.7% was achieved with a bilayer-structured back electrode, which included a layer of 10 wt% Ni-doped natural graphite (10Ni-G) for interfacial charge extraction.[104]

C-PSCs based on HTL-free and organic/inorganic HTLs

By combining cost-effectiveness and high stability, HTM-free C-PSCs are among the most promising solar cells for commercialization, yet their stability lags behind the state-of-the art HTM-based PSCs.[72,73] C-PSCs without HTMs can be classified into two main categories based on the type of carbon electrode: mesoscopic carbon electrodes and flat carbon electrodes. Typical HTM-free mesoscopic C-PSCs with a monolithic structure include a triple-layer mesoscopic design comprising TiO_2, ZrO_2, and carbon.[100,101,115–117,159–161,165–170] Alternatively, planar HTM-free C-PSCs employ layer-by-layer structures, such as FTO/TiO_2/perovskite/C or ITO/SnO_2/perovskite/C.[157,171]

The interface between the perovskite layer and the carbon electrode is critical for enhancing PCE and stability in C-PSCs. Surface modification techniques using materials such as polylactic acid (PLA) with carbonyl (C=O) groups, CQDs,[149] fluorine-doped CQDs (FCQDs),[150] ionic liquids such as 4-(dimethylamino)-1-(2,2,2-trifluoroacetyl)pyridin-1-ium 2,2,2-trifluoroacetate (DTPT),[151] CNTs,[154] potassium iodide (KI),[155] and cesium acetate (CsAc)[156] have been shown to improve hole injection and enhance device performance. For example, PLA-modified HTM-free PSCs have achieved a PCE of 14.70% for a 1 cm^2 device, one of the highest reported for a HTM-free C-PSC.[152]

Although HTM-free C-PSCs have shown promising stability, incorporating HTMs can further improve the hole extraction efficiency.[41] In particular, HTMs in C-PSCs contribute to two main benefits: (1) enhanced energy level alignment at the perovskite/carbon electrode interface, facilitating efficient hole extraction and reducing electron backflow; and (2) additional stability since hydrophobic and thermally stable HTMs protect C-PSCs from environmental degradation.[172]

Most HTMs used in C-PSCs are organic materials such as spiro-OMeTAD[163,164] and poly(3-hexylthiophene) (P3HT).[103,162,173] P3HT is particularly advantageous due to its low cost, simple manufacturing, dopant-free oxidation process, hydrophobic properties, and high thermal stability.[172] Over the past eight years, the PCE of large-area C-PSCs with organic HTLs has increased from 7.3%[174] to 17.02% for an active area of 1 cm^2.[163] A composite of P3HT and graphene as an HTL resulted in a record PCE of 17.05% for an active area of 50 cm^2.[103]

Despite progress with organic HTLs, challenges such as interfacial diffusion and stability issues have driven interest in inorganic HTLs for C-PSCs.[175] Inorganic or hybrid organic/inorganic HTLs, including materials like cobalt oxide (Co_3O_4),[176] copper-doped nickel oxide (Cu:NiO_x),[177] and copper iodide (CuI),[178] offer significant advantages, such as low cost, higher thermal and chemical stability, and solution processability. These materials also feature wide bandgaps and high optical transmittance, making them ideal for perovskite integration.[31] The combination of carbon-based electrodes with inorganic HTLs has shown exceptional potential for improving both performance and stability. For instance, integrating a CuI HTL with a carbon counter electrode in a large-area module (8 cm^2 active area) achieved a PCE of 15.9%, along with superior stability compared to non-sulfurized devices.[178]

Challenges of C-PSCs

Utilizing carbon-based materials shows significant potential in enhancing PSC performances, maximizing charge transfer while minimizing unwanted charge recombination, and boosting stability, while reducing manufacturing costs. Table 1 summarizes the results achieved for C-PSCs in the relevant literature. A standardized benchmark is needed to accurately compare PSCs made with different carbon materials.[185] Additionally, the inherent characteristics of certain carbon materials, such as conductivity and structural properties (whether amorphous or ordered), limit the performance of PSCs.[39] Air-stable PSCs can benefit greatly from carbon electrodes with thermal stability and water resistance. However, the PCE values of C-PSCs still lag behind those of advanced PSCs that incorporate HTLs and metal electrodes.[186] Graphite and carbon black, commonly used as the carbon electrode material in C-PSCs, suffer from poor hole selectivity because their Fermi level only slightly aligns with the valence band of the perovskite, leading to significant recombination loss. Additionally, a limited number of studies have reported using carbon electrodes that incorporate electron selectivity. Inadequate contact between the carbon electrode and the perovskite, as well as limitations in the fabrication methods, further hinder performance by causing unwanted charge recombination and reducing the PCE.[187] To improve C-PSCs, interfacial engineering must be employed to address these contact issues and enhance the extraction of photogenerated charge from the perovskite to the carbon electrode.[187] Another key challenge in using carbon-based materials to achieve optimal efficiency and durability is the lack of a thorough understanding of the fundamental processes required for industrial-scale production of the resulting devices. Moreover, despite the potential of carbon-based materials, they alone cannot fully address all stability issues in PSCs. Intrinsic factors such as ion migration, interfacial reactions, and the thermal instability of most perovskites contribute significantly to the degradation of PSCs.[188,189] Ion migration remains a major obstacle to extending the lifespan of these cells.[190] Defective sites, grain boundaries, and interfaces exacerbate this problem by promoting degradation through the interaction of mobile ions with electrons and holes.[190] The tendency of perovskite molecules to decompose into their original components, such as MAX and PbX_2 (where X = I, Br, Cl), also poses a threat to long-term stability. Another concern is the thermal instability of perovskites, which is driven by chemical and structural instabilities that have yet to be fully

Table 1 Reported device stack configuration, type of carbon, carbon electrode deposition technique, PV parameters, and stability test results for large-area (1.00 cm^2) C-PSCs

Cell configuration	Type of carbon	C electrode deposition method	J_{SC} [mA cm^{-2}]	V_{OC} [V]	FF	PCE [%]	Stability tests	Publication year	Ref.
FTO/TiO_2/$CsPbBr_3$/carbon	Commercial carbon paste	Screen printing	7.57	1.43	0.74	8.00	93.2% PCE retention after 30 days at 20 °C, ~40% relative humidity (RH)	2023	121
PEN/ITO/SnO_2/$CsPbBr_3$/carbon	Commercial carbon paste	Screen printing	7.50	1.49	0.74	8.27	93.2% PCE retention after 30 days at 20 °C, ~40% RH, 76% PCE retention after 1000 bending cycles	2023	121
PEN/CNT/Graphene/SnO_2/$MAPbI_3$/carbon	CNTs and low-concentration graphene	Hot-pressing	18.83	0.96	0.57	10.38	~90% PCE retention after ambient atmosphere storage for one month, ~71% PCE retention after 4000 bending cycles, 4 mm bending radius	2023	122
Ti/c-TiO_2/$MAPbI_3$/PTAA/graphene/PDMS	Graphene/PDMS	Lamination	18.70	1.08	0.74	15.0	Mechanical stability, bent 1000 times at $R = 12$, 8, and 4 mm	2018	120
FTO/TiO_2-NPs/$Cs_{0.17}FA_{0.83}Pb(I_{0.83}Br_{0.17})_3$/spiro-OMeTAD/carbon	Commercial carbon paste (JELCON CH-8)	Pressing	19.42	1.09	0.60	12.70	>80% PCE retention at 25 °C after 1000 h at 35–45% RH	2023	123
PEN/ITO/TiO_2-NPs/$Cs_{0.17}FA_{0.83}Pb(I_{0.83}Br_{0.17})_3$/spiro-OMeTAD/carbon	Commercial carbon paste (JELCON CH-8)	Pressing	17.18	1.03	0.50	8.80	>80% PCE retention after 1000 h at 25 °C, 35–45% RH, mechanical stability: 80% PCE retention, after 1000 bending cycles with bending radius of 17 mm	2023	123
PEN/ITO/SnO_2/PCBM/$Cs_{0.05}(FA_{0.85}MA_{0.15})_{0.95}Pb(I_{0.85}Br_{0.15})_3$/spiro-OMeTAD/carbon	Commercial carbon paste	Pressing	19.96	1.09	0.64	14.05	89% PCE retention after 1176 h, ambient conditions, 34% PCE retention after 1240 bending cycles, 10 mm bending radius, ambient conditions	2021	124
PET/IZO/PTAA/$Cs_{0.04}(FA_{0.83}MA_{0.17})_{0.96}Pb(I_{0.83}Br_{0.17})_3$/PCBM:PMMA/Cr/carbon	Carbon paste (DN-CP01)	Blade-coating	20.92	1.05	0.69	15.18	90% PCE retention for 1000 h at MPP, ~90% PCE retention after 1000 h at 85 °C	2020	125
PET/IZO/SnO_2/$Cs_{0.04}(FA_{0.83}MA_{0.17})_{0.96}Pb(I_{0.83}Br_{0.17})_3$/PTAA/Cr/carbon	Carbon paste (DN-CP01)	Blade-coating	19.49	1.02	0.61	12.06	90% PCE retention after 1000 h at MPP, ~90% PCE retention after 1000 h at 85 °C	2020	125
FTO/c,m-TiO_2/3D $Cs_{0.05}MA_{0.16}FA_{0.79}Pb(I_{0.84}Br_{0.16})_3$/2D PEA_2PbI_4/carbon	Carbon paste (FTU-16)	Screen printing	21.33	1.03	0.45	10.05	92% PCE retention after 1000 h at ~40% RH	2018	132

Table 1 (*Contd.*)

Cell configuration	Type of carbon	C electrode deposition method	J_{SC} [mA cm^{-2}]	V_{OC} [V]	FF	PCE [%]	Stability tests	Publication year	Ref.
FTO/c,m-TiO_2/ 3D $Cs_{0.09}MA_{0.14}FA_{0.77}Pb(I_{0.86}Br_{0.14})_3$/ 2D PEA_2PbI_4/carbon	LTC paste	Screen printing	18.37	0.98	0.65	11.76	~60% PCE retention after 1000 h at 24 °C, ~45% RH	2022	133
FTO/c,m-TiO_2/ 2D $(HOOC(CH_2)_2NH_3)_2PbI_4$/ 3D $MAPbI_3$/carbon	—	—	23.60	0.86	0.59	11.90	Stable for ~5000 h, 1 sun AM 1.5G	2016	134
FTO/c,m-TiO_2/ $Cs_x(MA_{0.17}FA_{0.83})_{(100-x)}Pb(I_{0.83}Br_{0.17})_3$/coal	Coal-C, acetylene black (AB), PVAc	Spray coating and doctor blade coating	22.29	0.89	0.44	8.72	Stable for 120 h at 30% RH	2019	139
FTO/c,m-TiO_2/ $Cs_{0.05}(MA_{0.17}FA_{0.83})_{0.95}Pb(I_{0.83}Br_{0.17})_3$/ bio-carbon (BC-B)	Bio-carbon, AB, PVAc	Spray coating and doctor blade coating	—	—	—	10.19	87% PCE retention after 2000 h at 25 °C, 30% RH	2020	140
FTO/c,m-TiO_2/ $MAPbI_3$/*N*-KSDC/carbon	1. Carbon paste (*N*-KSDC, CB and PMMA) 2. Pure carbon paste	1. Spraying 2. Doctor blade coating	21.00	1.02	0.52	11.08	92% PCE retention after 62 days at 25–35% RH	2022	141
FTO/SnO_2/ $CS_{0.05}(MA_{0.15}FA_{0.85})_{0.95}Pb(I_{0.85}Br_{0.15})_3$: O-MWCNTs/MWCNT	MWCNT	Spraying	21.96	0.996	0.41	8.99	80% PCE retention after 500 h at 30 °C, 40% RH	2020	142
FTO/SnO_2/ $Cs_{0.05}(MA_{0.15}FA_{0.85})_{0.95}Pb(I_{0.85}Br_{0.15})_3$/MWCNT	MWCNT	Spray coating	22.01	1.009	0.50	11.20	Stable for 600 h at ~30 °C, ~60% RH	2021	143
FTO/c-TiO_2/ $MAPbI_2Cl$/NiO@CSs	NiO@CSs (carbon spheres)	Doctor blade coating	22.06	0.84	0.63	11.70	Stable for 1500 h at 25 °C, 40%–60% RH	2019	144
FTO/c,m-TiO_2/ $MAPbI_3$/NiO-C&C	Commercial carbon paste and NiO nanocrystals	Doctor blade coating	21.2	1.038	0.57	12.5	>98% PCE retention after 720 h at >40% RH	2019	145
FTO/TiO_2/$MAPbI_3$/ B-rGO paper/FTO	Boron-doped rGO paper	Stacking	16.74	0.88	0.60	8.96	Stable for 250 h at RT, 60% RH	2018	99
FTO/c,m-TiO_2/ $Cs_{0.05}(FA_{0.85}MA_{0.15})_{0.95}Pb(I_{0.85}Br_{0.15})_3$/ spiro-OMeTAD/carbon	Graphene-based carbon paste	Spin coating	—	—	—	13.85	>93% PCE retention after 360 h, shelf life at ambient temperature and constant low RH	2021	42
FTO/SnO_2/$Cs_{0.05}(FA_{0.85}MA_{0.15})_{0.95}Pb(I_{0.85}Br_{0.15})_3$/ spiro-OMeTAD/carbon	Graphene-based carbon paste	Spin coating	—	—	—	14.06	>93% PCE retention after 360 h, shelf life at ambient temperature and constant low RH	2021	42

Table 1 (*Contd.*)

Cell configuration	Type of carbon	C electrode deposition method	J_{SC} [mA cm^{-2}]	V_{OC} [V]	FF	PCE [%]	Stability tests	Publication year	Ref.
FTO/c-TiO_2/$CsPbI_3$/spiro-OMeTAD/carbon	Graphite, macroporous carbon	Doctor blade coating	19.71	1.17	0.79	18.14	Tested under a steady-state bias voltage (0.95 V) and white LED illumination (initial cell current density 20 mA cm^{-2}) in N_2 atmosphere. No PCE degradation	2025	146
FTO/c,m-TiO_2/$PbTiO_3$/$MAPbI_3$/CNT	CNT	Spray coating	20.09	0.97	0.62	12.08	95% PCE retention for 90 days, at 25 °C, ~20% RH	2018	147
FTO/SnO_2/$FAPbI_3$/spiro-OMeTAD/10Ni-G/alloy bilayer	10 wt% Ni-doped graphite (10Ni-G)	Painting	23.9	1.04	0.75	18.7	Ambient storage stability: 85% PCE retention after >2000 h at 40–50% RH. Thermal stability: 86% PCE retention for 196 h at 70 °C, operational stability: ~86% PCE retention after 500 h at 10–20% RH, AM 1.5G illumination (100 mW cm^{-2})	2023	104
FTO/c,m-TiO_2/$CsPbBr_3$/carbon	Commercial carbon paste	Painting	7.24	1.45	0.74	7.81	92.8% PCE retention after 1650 h at 80 °C, 91.9% PCE retention after 984 h under continues illumination with a light intensity of 100 mW cm^{-2}, 84.6% PCE retention after 984 h under high humidity environment (around 75% RH)	2023	148
FTO/c,m-TiO_2/$MAPbI_3$(-CQDs)/carbon	Commercial carbon paste	Doctor blade coating	21.5	1.028	0.60	13.3	>95% PCE retention after 1000 h, at 40% RH	2019	149
FTO/c,m-TiO_2/$CsPbI_{2.5}Br_{0.5}$/FCQDs GHJ/carbon	Carbon paste	Doctor blade coating	16.87	1.12	0.72	13.53	>90% PCE retention after 1056 h at 85 °C	2021	150
FTO/TiO_2/DTPT/$CsPbBr_3$/DTPT/carbon	Commercial carbon paste	Blade coating	7.81	1.509	0.78	9.18	>91% PCE retention after 100 days, at ~55% RH	2023	151
ITO/SnO_2/ZnO/$CsPbI_{2.25}Br_{0.75}$/PLA/carbon	Commercial carbon paste	Painting	15.42	1.253	0.76	14.70	92% PCE retention after 62 days in air at 15–20% RH	2023	152
FTO/TiO_2-MXene/$CsPbI_2Br$/carbon	—	—	—	—	—	13.06	Ambient stability: 91% PCE retention, after 1250 h at 20–30% RH, 85% PCE retention after >400 h at 85 °C in a nitrogen atmosphere	2023	153
FTO/c,m-TiO_2/$Cs_{0.06}(MA_{0.17}FA_{0.83})Pb(I_{0.84}Br_{0.16})_3$:MWCNTs/carbon	Carbon paste (FTU-16)	Screen-printing	17.57	0.99	0.47	8.18	Stable at 30 °C, 50% RH for the first 2 h and 80% RH for the next 2 h	2017	154
FTO/SnO_2/$Cs_{0.05}(MA_{0.17}FA_{0.83})_{0.95}Pb(I_{0.83}Br_{0.17})_3$:KI/carbon	LTC paste (Dyenamo DN-CP01)	Blade coating	16.67	1.08	0.53	9.37	80% PCE retention after 414 h, 85 °C in a static oven with constant low RH	2020	155

Table 1 (*Contd.*)

Cell configuration	Type of carbon	C electrode deposition method	J_{SC} [mA cm^{-2}]	V_{OC} [V]	FF	PCE [%]	Stability tests	Publication year	Ref.
FTO/c,m-TiO_2/$MAPbI_3$ + $MA_{1-x}Cs_xPbI_3$/carbon	Carbon paste (graphite, CB, cellulose)	Doctor blade coating	—	—	—	13.04	Stable for 4 months at ∼50% RH	2019	156
ITO/SnO_2/$MAPbI_3$/carbon	Carbon paste	Screen printing	18.64	1.03	0.44	8.38	—	2023	157
FTO/c,m-TiO_2/m-ZrO_2/ HTC/$MAPbI_3$-AVA/LTC	HTC pastes, and LTC pastes	Screen printing	22.84	0.959	0.64	13.99	—	2021	101
FTO/c,m-TiO_2/$MAPbI_3$/Carbon	Commercial carbon paste	Printing	19.63	0.99	0.50	9.72	—	2016	158
FTO/c,m-TiO_2/m-ZrO_2/ m-carbon/$MAPbI_3$	Commercial carbon paste	Screen printing	—	—	—	9.8	Stable for 160 h, 18–22 °C, ∼50% RH, illumination from white LEDs at 0.5 equivalent sun	2017	159
FTO/c,m-TiO_2/m-ZrO_2/ m-carbon/$MAPbI_3$-AVA	Commercial carbon paste	Screen printing	23.26	0.9	0.63	13.11	—	2022	160
FTO/c,m-TiO_2/m-ZrO_2/ m-carbon/$MAPbI_3$-AVA	Commercial carbon paste	Printing	23.87	0.89	0.65	13.82	80% PCE retention after > 420 h at 50 °C, 30–40% RH	2022	161
FTO/c,m-TiO_2/$CsPbI_2Br$/ P3HT-MWCNT/Carbon	Carbon paste (CB, graphite, α-terpineol)	Doctor blade coating	11.71	1.19	0.54	7.52	∼85% PCE retention after 240 h at ∼35% RH	2019	162
FTO/c-SnO_2/ $Cs_{0.05}(FA_{0.85}MA_{0.15})_{0.95}$ $Pb(I_{0.85}Br_{0.15})_3$/spiro-OMeTAD/ carbon	Commercial carbon paste	Pressing	20.94	1.130	0.72	17.02	90.5% PCE retention after 1500 h at 20 °C, 30% RH	2020	163
FTO/ZnO/ $Cs_{0.17}FA_{0.83}Pb(I_{0.83}Br_{0.17})_3$/ Spiro-OMeTAD/carbon	Commercial carbon paste	Hot-pressing	17.1	1.05	0.59	10.7	—	2022	164

Table 2 Reported device stack configuration, type of carbon, carbon electrode deposition technique, number of interconnected cells, PV parameters and stability test results for large-area (>1.00 cm^2) C-PSCs

Stack configuration	Type of carbon	C electrode deposition method	Active area (cm^2)	Number of interconnected cells	J_{SC} [mA cm^{-2}]	V_{OC} [V]	FF	PCE [%]	Stability tests	Publication year	Ref.
ITO/SnO_2/$FA_{0.88}Cs_{0.12}PbI_3$/Spiro-OMeTAD/carbon	Commercial carbon paste	Lamination	5.5 cm^2	—	22.3	1.11	68.2	16.9%	84% PCE retention after 1000 h, 25 °C, 40–80% RH	2024	80
FTO/c-TiO_2/m-TiO_2/m-ZrO_2/m-carbon/TFPbI$_3$–MAPbI$_3$	Carbon slurry (CB, graphite, terpineol, ethyl cellulose)	Screen printing	11.8	6	3.82	5.33	0.613	12.48	90% PCE retention after 1000 h at MPP	2022	135
FTO/c-TiO_2/m-TiO_2/m-Al_2O_3/m-carbon/$FA_xMA_{(1-x)}PbI_yBr_{(3-y)}$	Commercial carbon paste	Printing	4	2	—	1.86	0.49	6.30	64% PCE retention after 1000 h, 23 °C, 40% RH	2023	136
FTO/c-TiO_2/m-TiO_2/m-ZrO_2/m-carbon/$(5\text{-AVA})_x(MA)_{1-x}PbI_3$	Carbon paste (graphite, CB, PVDF and terpineol)	Doctor blade coating	1.2	—	12.54	1.04	0.59	7.69	Stable for ~ 10 days, under AM1.5G solar illumination in air	2020	137
FTO/c-TiO_2/m-TiO_2/m-ZrO_2/m-carbon/$HOOC(CH_2)_4NH_3)_2PbI_4$/$MAPbI_3$	Carbon black/graphite slurry	Printing	47.6 (10 × 10 cm^2)	7	2.247	7.05	0.704	11.2	100% PCE retention after 12 000 h at 1 sun AM 1.5G conditions and 55 °C	2017	53
FTO/SnO_2/m-TiO_2/$(EDBEPbI_4)_{0.03}[Cs_{0.05}(FA_{0.83}MA_{0.17})_{0.95}Pb(I_{0.83}Br_{0.17})_3]_{0.97}$/Spiro-OMeTAD/carbon	Carbon paddle	Screen printing	342 (6 × 57 cm^2)	6	15.12	6.46	0.71	11.59	90% PCE retention after 3 months (3000 + h) in air	2018	138
ITO/SnO_2/$(FAPbI_3)_{0.95}(MAPbBr_3)_{0.05}$/CLP/4F-$PEA_2PbI_4$/Spiro-OMeTAD/carbon	Carbon paste (graphite, CB, PA and additive)	Hot-pressing	17.1	6	66.2	6.73	0.751	19.6	90% PCE retention after 4390 h at 60 °C	2023	105
FTO/SnO_2/FAMAPbIBr/Spiro-OMeTAD/graphene	Graphene	Spraying	1.30	—	22.48	1.16	0.63	16.42	90% PCE retention after 1000 h at 85 °C, 40–80% RH, N_2 atmosphere	2019	102
FTO/c,m-TiO_2/$MAPbI_{3-x}Cl_x$/GC@$MAPbI_{3-x}Cl_x$	Naturally extracted graphitic carbon (naturally extracted graphitic carbon, CB and α-terpineol)	Brush painting	88 (10 × 10 cm^2)	—	14.29	0.90	0.49	6.32	Air stability: 80% PCE retention after 30 days at ~23 ± 5 °C, 77 ± 5% RH, photostability: 80% PCE retention after 6 days at 1 sun light-soaking illumination	2022	98

Table 2 (*Contd.*)

Stack configuration	Type of carbon	C electrode deposition method	Active area (cm^2)	Number of interconnected cells	J_{SC} [mA cm^{-2}]	V_{OC} [V]	FF	PCE [%]	Stability tests	Publication year	Ref.
FTO/c,m-TiO_2/$Cs_{0.05}(MA_{0.17}FA_{0.83})_{0.95}Pb(I_{0.83}Br_{0.17})_3$/PEAI/HTL/carbon	Commercial carbon paste	Blade coating	6.25	—	—	—	—	8.36	—	2023	179
FTO/c-TiO_2/m-TiO_2/m-ZrO_2/Co_3O_4/Carbon/$MAPbI_3$-AVA	Commercial carbon paste	Printing	70	—	22.10	9.15	0.57	11.39	Stable for 100 days, at 25 °C, ~70% RH	2018	176
FTO/c-TiO_2/m-TiO_2/m-ZrO_2/Cu:NiO_x/NiO_x/Carbon/$MAPbI_3$-AVA	Carbon paste	Printing	70	10	153.2 (I_{SC})	9.57	0.59	12.10	Stable for >4500 h at 25 °C, 65% RH	2019	177
FTO/ZTO-ZnS/$Cs_{0.05}(FA_{0.85}MA_{0.15})_{0.95}Pb(Br_{0.15}I_{0.85})_3$/CuI/carbon	Commercial carbon paste	Pressing	8 (4 × 4 cm^2)	4	5.33	4.28	0.695	15.9	>85% PCE retention after 1000 h at 85 °C, 85% RH	2021	178
ITO/SnO_2/$MA_{0.9}GA_{0.1}PbI_3$/P3HT/Ta-WO_x/carbon	Commercial carbon paste	Blade coating	4 (25 cm^2)	4	21.2	1.05	0.690	15.3	100% PCE retention after 5000 h, thermal stability at 85 °C in nitrogen-filled glovebox	2021	180
FTO/c,m-TiO_2/$MAPbI_3$/carbon	Carbon paste (graphite, CB, TTIP and HAC)	Screen printing	34.2 (3 × 11.4 cm^2)	3	19.47	0.89	0.47	9.09	>95% PCE retention after 1000 h of dark storage ageing, low upscaling losses (8.1%$_{rel}$ dec^{-1} of upscaled active area)	2022	181
FTO/m-TiO_2/m-ZrO_2/m-carbon/(5-AVA)$_x$(MA)$_{1-x}PbI_3$	Commercial carbon paste	Screen printing	60.08 (10 × 10 cm^2)	9	150.18 (I_{SC})	8.50	0.61	12.87	—	2020	165
FTO/c-TiO_2/m-TiO_2/m-ZrO_2/Carbon/$MAPbI_3$-AVA	Commercial carbon paste	Screen printing	11.7	6	3.65	5.11	0.59	11.05	Stable for 700 h at ~21 °C, 1 sun illumination	2020	166
ITO/HMB-doped C_{60}/$MAPbI_3$/carbon	Commercial carbon paste	Doctor blade coating	4 (3.2 × 3.2 cm^2)	—	20.13	1.02	0.51	10.48	Humidity stability: 81.9% PCE retention after 60 days, photostability, 90% PCE retention after 338 h, 20–30% RH, at MPP under 1 sun illumination	2019	182
ITO/SnO_2/FABr + $MAPbI_3$+FAI/carbon	Commercial carbon paste	Blade coating	1.13	—	20.84	1.04	0.63	13.72	96% PCE retention after 60 days, 20 ± 5 °C, 20–80% RH	2023	171
FTO/c-TiO_2/m-TiO_2/m-ZrO_2/m-carbon/(5-AVA)$_x$(MA)$_{1-x}PbI_3$	Carbon/graphite paste	Screen printing	56.8 (10 × 10 cm^2)	12	—	—	—	11.1	—	2022	167

Table 2 (*Contd.*)

Stack configuration	Type of carbon	C electrode deposition method	Active area (cm^2)	Number of interconnected cells	J_{SC} [mA cm^{-2}]	V_{OC} [V]	FF	PCE [%]	Stability tests	Publication year	Ref.
FTO/c,m-TiO_2/$MAPbI_3$/carbon	Carbon paste	Doctor blade coating	52 (10 × 10 cm^2)	9	91.1 (I_{SC})	10.0	0.58	10.2	95% PCE retention after 500 h, 40% RH	2019	183
FTO/ZnO/$MAPbI_3$/carbon	Carbon paste	Screen printing	17.6 (5 × 5 cm^2)	8	3.25	6.14	0.53	10.6	Stable after 140 days of outdoor testing	2017	114
FTO/c-TiO_2/m-TiO_2/m-ZrO_2/m-carbon/$MAPbI_3$-AVA	Commercial carbon paste	Screen printing	198	22	192 (I_{SC})	19.7	0.34	6.6	100% PCE retention after hundreds of hours at 70% RH, PCE as high as 6.6% (6.3% stabilized) after 2 months since fabrication	2018	117
FTO/c-TiO_2/m-TiO_2/m-ZrO_2/m-carbon/$MAPbI_3$-AVA	Carbon paste	Screen-printing	220	22	20.30	0.96	0.44	8.5	Humidity treatments for 16 h in an oven at 25 °C and 70% RH, 6.4% PCE increase	2024	168
FTO/c-TiO_2/m-TiO_2/m-ZrO_2/m-carbon/$(5\text{-AVA})_x MA_{1-x} PbI_3$	Carbon paste	Lamination	1.5	—	12 to 20	Drop 0.82 Ink 0.91	Drop 0.62 Ink 0.75	Drop 6 Ink 9	Drop-casting perovskite, 8% PCE at 1000 h and 4% at 3000 h of aging, inkjet printing perovskite, poor stability, with no functional cells remaining at 1000 h of aging	2024	169
FTO/c-TiO_2/m-TiO_2/m-ZrO_2/m-carbon/$(5\text{-AVA})_x(MA)_{1-x}PbI_3$	Carbon-graphite paste	Screen printing	49 (10 × 10 cm^2)	10	2.0	9.3	0.56	10.4	Light-soaking stability: 100% PCE retention after 1000 h, 25 °C, 54% RH, outdoor stability: 100% PCE retention after 1 month, 30 °C, 80% humidity shelf-life stability: 100% PCE retention over 1 year in dark	2017	115
FTO/c-TiO_2/m-TiO_2/m-ZrO_2/m-carbon/$MAPbI_3$-AVA	Commercial carbon paste	Printing	31 (10 × 5 cm^2)	4	19.6	3.72	0.57	10.46	Stable for 2000 h at 25–30 °C, 65–70% RH	2016	116
FTO/c-TiO_2/m-TiO_2/m-ZrO_2/m-carbon/$MAPbI_3$-AVA	Commercial carbon paste	Printing	70 (10 × 10 cm^2)	10	17.72	9.63	0.63	10.74	Stable for 2000h shelf life, 25–30 °C, 65–70% RH	2016	116
				10	22.62	9.12	0.56	11.55		2020	170

Table 2 (*Contd.*)

Stack configuration	Type of carbon	C electrode deposition method	Active area (cm^2)	Number of interconnected cells	J_{SC} [mA cm^{-2}]	V_{OC} [V]	FF	PCE [%]	Stability tests	Publication year	Ref.
FTO/c-TiO_2/m-TiO_2+CsBr/m-ZrO_2/Carbon/$MAPbI_3$-AVA	Commercial carbon paste	Screen printing	70 (10 × 10 cm^2)						Stable for 2700 h at 25 °C, 65−70% RH, stable for 750 h at 85 °C		
FTO/c-TiO_2/m-TiO_2/m-ZrO_2/Carbon/GT+TU+U-$MAPbI_3$	Commercial carbon paste	Casting	51.5	9	2.20	8.48	0.62	11.6	100% PCE retention after 2000 h in a desiccator and under an ambient atmosphere	2023	100
FTO/SnO_2/$(FAPbI_3)_{0.98}(MAPbBr_3)_{0.02}$/P3HT/carbon	Commercial carbon paste	Blade coating	12 (5 × 5 cm^2)	6	3.47	6.133	0.63	13.20	96% PCE retention for 3600 h under dark conditions at ∼25 °C, 20% RH, 88% PCE retention for 1200 h at 70 °C	2023	173
FTO/c-TiO_2/m-TiO_2/m-ZrO_2/m-carbon/$(5\text{-AVA})_xMA_{1-x}PbI_3$	Graphite	Screen-printing	1.5 (aperture area of 0.64 cm^2)	—	13	0.90	0.6	7.3	85% PCE retention for 1029 h, RH of 85% and RT, 40 °C (keeping constant RH	2024	174
FTO/c,m-TiO_2/$MAPbI_{3-x}Cl_x$/carbon + MAI/Carbon	Commercial carbon paste	Doctor blade coating	>1.1	—	21.47	0.996	0.61	13.04	Air stability: >90% PCE retention after 160 days, water stability: >60% PCE retention for 160 days	2017	184
ITO/SnO_2/$MA_{0.65}FA_{0.35}PbI_3$/P3HT@graphene/carbon	Carbon slurry	Blade coating	50 (10 × 10 cm^2)	10	2.37	10.75	0.67	17.05	PCE increased by 1.4% after half a year at 25 ± 5 °C, 50 ± 5% RH	2023	103
ITO/SnO_2/$MA_{0.65}FA_{0.35}PbI_3$/Carbon	Carbon slurry	Blade coating	50 (10 × 10 cm^2)	10	2.45	10.46	0.60	15.26	—		103

addressed. Certain perovskites experience phase and structural changes within the temperature range critical for PV use, particularly under full sunlight conditions (above 85 °C).[185,191] As soft materials, perovskites are highly responsive to even small temperature changes, which further complicates their application in long-lasting PV systems.[192]

Prospects of C-PSMs

The growing interest in the use of carbon electrodes in PSMs is reflected in the growing body of research over the past five years.[47] Table 2 summarizes the PV characteristics measured for C-PSMs, as reported in the relevant literature. Fig. 8 reports the PCEs of large-area C-PSCs and C-PSMs as a function of active area. While the integration of carbon electrodes in PSMs shows promise for moving the technology towards commercial viability, several technical aspects must be considered to ensure the economic feasibility of C-PSMs as a competitive product. The main areas for further study and improvement include the following: (i) Film uniformity and scaling: one major obstacle in scaling C-PSMs is the decline in PCE when transitioning from lab-scale solar cells to large modules. Achieving uniform coatings on large surfaces using cost-effective methods such as printing remains a significant challenge, particularly with the perovskite layer, which has the greatest impact on device performance.[47] Research should focus on optimizing deposition and annealing techniques to create high-quality films under ambient conditions. Applying chemical modifications and engineering methods from previous thin-film technologies could help achieve this goal, leading to uniform CTLs and perovskite films that enhance the PCE and reduce production costs. These achievements will make C-PSMs competitive with silicon-based solar modules.[47] (ii) Improved cell connection: as PSMs are scaled up, the way cells are interconnected, typically through scribing, directly affects the geometric fill factor (gFF), a crucial determinant of module PCE. Laser scribing has emerged as a promising technology that can enhance performance when used alongside monolithic module fabrication techniques such as screen printing. Advances in laser technology can improve the precision of scribing, leading to higher gFF values, improved PCE, and minimized scaling losses.[47] (iii) Encapsulation for stability: effective encapsulation strategies are critical for ensuring that PSMs can achieve lifetimes comparable to commercially available PV products, which typically last a decade or more. However, due to the multiple layers within C-PSMs, each responding differently to temperature and chemical exposure, further research is needed. The perovskite layer and several CTLs are highly susceptible to degradation, requiring innovative solutions to ensure module longevity. Addressing these encapsulation and stability challenges will be crucial in enabling C-PSMs to enter the PV market in the near future.[47,193] Overcoming these obstacles will be key to unlocking the full potential of C-PSMs for commercial applications.

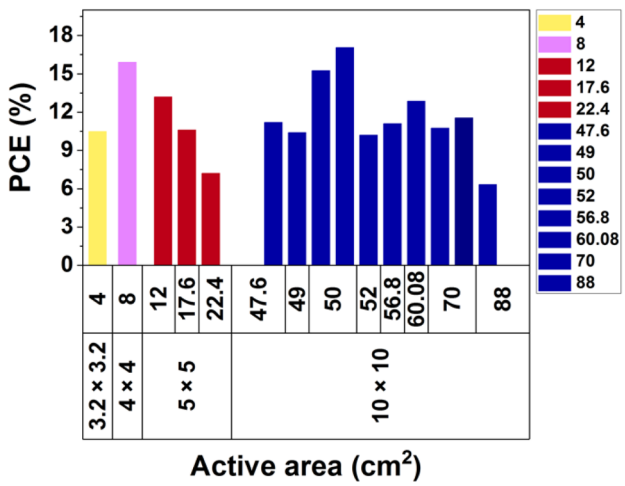

Fig. 8 Scaling-up process of C-PSCs. PCEs of large-area C-PSCs and C-PSMs as a function of active area.

Cost analysis

Perovskite solar cells based on carbon electrodes are under active investigation, where the counter electrode is replaced by a cost-effective carbon electrode, typically deposited as a carbon paste using different deposition methods.[47] The cost of carbon materials is substantially lower than that of metals, *e.g.*, carbon black costs around USD 20 kg^{-1}, compared with USD 60 000 kg^{-1} for Au, USD 3083 kg^{-1} for Ag, and USD 633 kg^{-1} for Cu, making carbon a suitable choice for low-cost PSC fabrication.[194] At present, high-purity micronised graphite is priced around USD 3650 per metric ton, while gold is priced at over USD 63.9 million per metric ton, resulting in a price difference of approximately 18 000-fold.[195] Nevertheless, the amount of material required for such electrodes must also be considered in the overall cost balance. The manufacturing costs of including standard PSCs, inverted PSCs, and HTL-free C-PSCs (1 m^2) were calculated and compared in detail by Li *et al.*,[196] taking into account material costs, equipment depreciation, and energy consumption, independent of efficiency and stability. By substituting the metal electrode and HTL with a carbon electrode, the production costs for C-PSCs were significantly reduced compared to the other two PSC types. Specifically, the overall cost decreased from \$86.49 and \$81.31 to \$41.16, corresponding to a cost reduction of 49–52%, thereby making C-PSCs a strong candidate for next-generation, cost-effective PV technology.[195] To ensure sufficient conductivity, the carbon paste layer is typically ~20 μm thick, which is much thicker than a metal counter electrode. Nevertheless, because carbon paste costs only \$0.01 g^{-1} (equivalent to about 1.4% of the cost of Ag at \$0.71 g^{-1}), the material cost of carbon electrodes is significantly lower than that of Ag electrodes. Consequently, the overall material cost of C-PSCs amounts to about \$15.04. Calculations further indicate that the material cost of C-PSCs is reduced by about 69.7% and 66.2% compared to standard and inverted PSCs, respectively.[195] A representative study by Kajal utilized bottom-up cost modeling to analyze the production costs of C-PSMs.[197] Two module types were considered: high-temperature (Module A) and low-temperature (Module B).

Each module was designed at 1 m^2 scale with 20 monolithically integrated cells and a PCE equal to 75% of the corresponding lab-scale device, accounting for losses when scaling from a small area to a large area.[47] The average production cost was estimated at 0.21 USD per W and 0.15 USD per W for Modules A and B, respectively. The corresponding LCOE (levelized cost of energy) ranged from 0.034 to 0.016 USD per kWh for Module A and from 0.030 to 0.014 USD per kWh for Module B, assuming an operational lifetime of 10–25 years with 80% of the initial PCE retained.[47] Their analysis also revealed that the cost of starting materials significantly influences overall module economics. For Module A, ZrO_2 was identified as the primary cost driver, whereas Module B showed the highest sensitivity to variations in multiple factors.[47] Additional studies confirm the cost advantage of carbon-based architectures. Cai *et al.* designed two types of PSMs: a high-temperature carbon-based PSM [FTO/c,m-TiO_2/ZrO_2/C with $CH_3NH_3PbI_{(3-x)}(BF_4)_x$] and a high-precision, high-efficiency PSM [ITO/PEDOT:PSS/perovskite/PCBM/Ca/Al], and concluded that carbon-based PSCs offered lower production costs.[198] Chang *et al.* assessed three glass-based PSM structures FTO/c-TiO_2/perovskite/P3HT/Au, FTO/c-TiO_2/perovskite/P3HT/Ag, and FTO/c-TiO_2/perovskite/P3HT/Ag, reporting estimated manufacturing costs of \$175, \$102, and \$90 m^{-2}, respectively.[197] Their analysis further indicated that production costs in China could range from \$87 to \$140 m^{-2}. Song *et al.*[199] examined three PSM designs, *i.e.*, single-junction, two-terminal, and four-terminal all-perovskite tandem, and found the module selling prices (MSPs) ranged from \$0.32 to \$0.37 W^{-1} for U.S. manufacturing. Li *et al.*[200] investigated four module variants, *i.e.*, Si PERC, planar PSM, silicon/perovskite tandem, and perovskite/perovskite tandem, achieving PCEs of 21%, 19%, 25%, and 22%, respectively. The corresponding production costs were \$89.59, \$32.69, \$121.18, and \$45.23 m^{-2}, with estimated LCOEs of 5.5, 4.34, 5.22, and 4.22 ¢ kWh^{-1}.[197] Overall, the estimated manufacturing cost for a 1 m^2 module is roughly USD 1800 for traditional PSCs and USD 900 for carbon-based, HTM-free devices. Although carbon-based PSCs generally exhibit ~30% lower efficiency than traditional PSCs, this drawback is compensated by their reduced production costs and improved stability, making HTM-free, carbon-based PSCs highly promising candidates for cost-effective and scalable photovoltaic fabrication.[201]

Integration of carbon electrodes into tandem perovskite solar cells

In tandem solar cells, carbon-based materials like graphene and CNTs play a crucial role in enhancing performance and stability. They replace traditional metal electrodes, offering high transparency, flexibility, and resistance to ion migration and sputtering damage.[202] Analogous to the cases in PSCs, nanocarbon materials can be used in Si-perovskite tandem solar cells as electrodes or interfacial layers. The first report was by Lang *et al.*[203] who demonstrated four-terminal tandem devices, where graphene was used as the contact material between the Au electrodes and the perovskite layer. Electrodes made from large-area CVD graphene combine a flexible transfer process with excellent optoelectronic properties, making them ideal for perovskite/silicon tandem solar cells exceeding the Shockley–Queisser limit. A transparent, high-quality single-layer graphene contact was successfully implemented in PSCs, achieving electrical performance comparable to standard Au contacts, with ~1 V of V_{OC} and identical charge collection efficiency. The spiro-OMeTAD/graphene electrode is thus suitable for both four-terminal and monolithic perovskite tandem solar cells.[203] In 2020, Lee *et al.*[204] used floating-catalyst-grown CNT electrodes in four-terminal Si-perovskite tandem solar cells for the first time. CNT electrode-laminated PSCs, when combined with n-type tunnel oxide passivated contact (TOPCon) silicon solar cells in a four-terminal tandem configuration, achieved a high power conversion efficiency of 24.42%. While CNT electrodes show higher infrared transmittance than ITO/MoO_x, optical simulations revealed lower actual transmittance due to total internal reflection and scattering. This study marks the use of CNT electrodes in tandem solar cells and demonstrates their advantages, including flexibility, absence of ion migration-induced degradation, high optical conductivity, and ease of transfer. Compared to graphene, which suffers from grain defects and low reproducibility despite its high transparency, CNT electrodes avoid such issues and offer exceptional mechanical stretchability and the potential for solution processing. Among the various silicon solar cell types tested, the n-type TOPCon Si bottom cell paired with a CNT-based PSC top cell delivered the best performance.[204] Hang *et al.*[205] demonstrated a four-terminal perovskite-graphene-Si tandem. Selecting a graphene/silicon heterojunction solar cell as a bottom cell enabled the entire fabrication to be easily and successfully performed at high temperatures of over 200 °C. CNT-based PSCs were proposed for silicon–perovskite tandem use, with COMSOL simulations predicting 23.7% PCE in a four-terminal configuration.[202] The optimized HTL-free semi-transparent carbon-based PSC, combined with a silicon bottom cell using current matching, achieved 28.62% PCE, V_{OC} of 2.138 V, J_{SC} of 15.60 mA cm^{-2}, and FF of 85.79%. This approach offers a simple, stable, and cost-effective route for efficient silicon/perovskite tandems.[206] A carbon-based all-perovskite tandem solar cell was investigated with the structure ITO/SnO_2, $Cs_{0.2}FA_{0.8}Pb(I_{0.7}Br_{0.3})_3$/$WS_2$/$MoO_3$/ITO/$C_{60}$, $MAPb_{0.5}Sn_{0.5}I_3$/PEDOT:PSS/carbon. The bandgap configuration of the cell was 1.75 eV/1.17 eV, corresponding to a theoretical efficiency limit of 36%. Our analysis demonstrates the effectiveness of embedding cubic plasmonic metallic nanoparticles of Au and Ag within the absorber layers, which reduces the need for thicker absorber layers while simultaneously lowering manufacturing costs and mitigating Pb toxicity.[207]

Conclusions and outlook

This review emphasizes the critical role of carbon electrodes in advancing PSCs. C-PSCs offer a pathway to more sustainable, scalable, and cost-effective perovskite-based PV technologies.

Through innovations in carbon pastes and deposition methods, devices with active areas up to 342 cm^2 now achieve operational PCEs rivalling those of metal-based counterparts,[138] with modules demonstrating PCEs exceeding 19.6% under real-world conditions.[105] The use of scalable fabrication techniques such as screen printing, doctor blade coating, and roll-to-roll processes has further enhanced the feasibility of large-area manufacturing, significantly reducing production costs. Additionally, the hydrophobic nature of carbon electrodes acts as an inherent moisture barrier, contributing to the remarkable stability of C-PSCs.

While carbon electrodes are pivotal, their full potential is realized through synergistic advancements in other layers. Innovations in perovskite deposition, including solvent engineering and compositional tuning, have produced defect-free films with enlarged grain sizes and minimized recombination losses. This ensures efficient charge extraction, leveraging the high conductivity of carbon electrodes. Interfacial engineering has also addressed mismatched energy levels, further enhancing device performance. Advances in interface engineering such as hydrophobic polymers and 2D/3D hybrid perovskite layers,[105] complement carbon electrodes by enhancing both stability and durability under harsh environmental conditions.

The use of advanced carbon composites has unlocked new performance benchmarks for C-PSCs. Materials like CNTs, graphene, and bio-derived carbons have shown promise in improving conductivity, reducing interfacial resistance, and enhancing mechanical stability.

Carbon electrodes are particularly well-suited for flexible and lightweight solar cells, addressing the demand for portable and wearable PV applications. FC-PSCs have achieved PCE of 16.9% with remarkable bending stability over thousands of cycles, highlighting their durability and mechanical adaptability.[80] These properties, combined with the compatibility of carbon electrodes with roll-to-roll printing, position perovskite-based PVs as frontrunners in emerging markets such as portable electronics, foldable displays, and BIPVs.

The inherent stability of carbon electrodes underpins the long-term viability of C-PSCs. Devices with carbon electrodes have demonstrated exceptional resistance to moisture and thermal degradation, with operational stability exceeding 10 000 h under ambient conditions. Advances in encapsulation and interfacial engineering have further enhanced this stability, ensuring that carbon-based modules can compete with silicon-based PVs in terms of durability. Modules operating under high humidity and elevated temperatures retain PCEs above 90% of their initial values, underscoring the resilience of carbon electrodes in real-world environments.

While significant progress has been made, challenges remain in optimizing carbon electrode interfaces to reduce recombination losses and improve work function alignment. The integration of laser-based patterning techniques for module interconnections also requires refinement to address thermal stresses and ensure precision in thick carbon electrode layers. Developing new carbon composites with tailored electrical and mechanical properties will be critical for enhancing device performance and scalability. Furthermore, addressing the intrinsic limitations of perovskite materials, such as ion migration and phase instability, will be key to unlocking the full potential of carbon-based devices. To accelerate the commercialization of C-PSCs, future research should focus on:

- *Interface optimization*: enhancing interfacial contact between carbon electrodes and perovskite layers through advanced surface treatments and functional additives.
- *Advanced carbon composites*: exploring hybrid carbon materials with enhanced conductivity, stability, and work function tunability.
- *High-throughput manufacturing*: scaling up fabrication processes, including roll-to-roll and slot-die coating, to achieve cost-effective production of large-area modules.
- *Long-term stability studies*: investigating degradation mechanisms under real-world conditions to develop robust encapsulation and stabilization strategies.

Overall, carbon electrodes are positioned to drive the next generation of sustainable and efficient PV technologies. By addressing the remaining challenges and synergizing advancements across all device layers, C-PSCs have the potential to deliver high-performance solar modules that rival conventional silicon-based systems, paving the way for a sustainable and energy-efficient future.

Conflicts of interest

There are no conflicts to declare.

Data availability

The review uses existing public datasets, which are cited in the article.

Acknowledgements

We would like to thank the EPFL Library for funding the open access publication of this article.

References

1 T. A. Chowdhury, *et al.*, Stability of perovskite solar cells: issues and prospects, *RSC Adv.*, 2023, **13**, 1787–1810, DOI: **10.1039/d2ra05903g**.
2 T. I. Alanazi, Current spray-coating approaches to manufacture perovskite solar cells, *Results Phys.*, 2023, **44**, 106144, DOI: **10.1016/j.rinp.2022.106144**.
3 Y. Chen, L. Zhang, Y. Zhang, H. Gao and H. Yan, Large-area perovskite solar cells - a review of recent progress and issues, *RSC Adv.*, 2018, **8**, 10489–10508, DOI: **10.1039/c8ra00384j**.
4 **https://www.iea.org/reports/electricity-2024/executive-summary**.
5 P. You, G. Tang and F. Yan, Two-dimensional materials in perovskite solar cells, *Mater. Today Energy*, 2019, **11**, 128–158, DOI: **10.1016/j.mtener.2018.11.006**.

6 X. Zhang, *et al.*, A review of integrated systems based on perovskite solar cells and energy storage units: fundamental, progresses, challenges, and perspectives, *Adv. Sci*, 2021, **8**, 2100552, DOI: **10.1002/advs.202100552**.
7 B. J. Kim, S. Lee and H. S. Jung, Recent progressive efforts in perovskite solar cells toward commercialization, *J. Mater. Chem. A*, 2018, **6**, 12215–12236, DOI: **10.1039/x0xx00000x**.
8 Y. Wang, *et al.*, High-efficiency flexible solar cells based on organometal halide perovskites, *Adv. Mater.*, 2016, **28**, 4532–4540, DOI: **10.1002/adma.201504260**.
9 S. L. Hamukwaya, *et al.*, A review of recent developments in preparation methods for large-area perovskite solar cells, *Coatings*, 2022, **12**, 252, DOI: **10.3390/coatings12020252**.
10 R. Wang, *et al.*, A review of perovskites solar cell stability, *Adv. Funct. Mater.*, 2019, **29**, 1808843, DOI: **10.1002/adfm.201808843**.
11 Q. Wali, *et al.*, Advances in stable and flexible perovskite solar cells, *Curr. Appl. Phys.*, 2020, **20**, 720–737, DOI: **10.1016/j.cap.2020.03.007**.
12 T. Leijtens, *et al.*, Stability of metal halide perovskite solar cells, *Adv. Energy Mater.*, 2015, **5**, 1500963, DOI: **10.1002/aenm.201500963**.
13 F. F. A. Di Giacomo, R. Jose and T. M. Brown, Progress, challenges and perspectives in flexible perovskite solar cells, *Energy Environ. Sci.*, 2016, **9**, 3007–3035, DOI: **10.1039/C6EE01137C**.
14 D. Yang, R. Yang, S. Priya and S. F. Liu, Recent advances in flexible perovskite solar cells: fabrication and applications, *Angew. Chem., Int. Ed.*, 2019, **58**, 4466–4483, DOI: **10.1002/anie.201809781**.
15 Z. Yang, *et al.*, Review on practical interface engineering of perovskite solar cells: from efficiency to stability, *Sol. RRL*, 2020, **4**, 1900257, DOI: **10.1002/solr.201900257**.
16 **https://www.nrel.gov/pv/assets/pdfs/best-research-cell-efficiencies.pdf**.
17 C. Ballif, F. J. Haug, M. Boccard, P. J. Verlinden and G. Hahn, Status and perspectives of crystalline silicon photovoltaics in research and industry, *Nat. Rev. Mater.*, 2022, **7**, 597–616, DOI: **10.1038/s41578-022-00423-2**.
18 Z. Sun, *et al.*, Toward Efficiency Limits of Crystalline Silicon Solar Cells: Recent Progress in High-Efficiency Silicon Heterojunction Solar Cells, *Adv. Energy Mater.*, 2022, **12**, 2200015, DOI: **10.1002/aenm.202200015**.
19 M. V. Dambhare, B. Butey and S. V. Moharil, A review of different types of solar cells and its future trends, *J. Phys.: Conf. Ser.*, 2021, **1913**, 012053, DOI: **10.1088/1742-6596/1913/1/012053**.
20 S. Bellani, *et al.*, Solution-processed two-dimensional materials for next-generation photovoltaics, *Chem. Soc. Rev.*, 2021, **50**, 11870–11965, DOI: **10.1039/d1cs00106j**.
21 S. D. B. George, A. Soosaimanickam and S. Sundaram in *Photovoltaics beyond Silicon*, 2024, pp. 75–110.
22 M. A. Green, *et al.*, Solar cell efficiency tables (Version 64), *Prog. Photovolt.: Res. Appl.*, 2024, **32**, 425–441, DOI: **10.1002/pip.3831**.
23 J. Ling, *et al.*, A perspective on the commercial viability of perovskite solar cells, *Sol. RRL*, 2021, **5**, 2100401, DOI: **10.1002/solr.202100401**.
24 Y. Ma, Z. Lu, X. Su, G. Zou and Q. Zhao, Recent progress toward commercialization of flexible perovskite solar cells: from materials and structures to mechanical stabilities, *Adv. Energy Sustainability Res.*, 2023, **4**, 2200133, DOI: **10.1002/aesr.202200133**.
25 E. Lamanna, *et al.*, Mechanically Stacked, Two-Terminal Graphene-Based Perovskite/Silicon Tandem Solar Cell with Efficiency over 26%, *Joule*, 2020, **4**, 865–881, DOI: **10.1016/j.joule.2020.01.015**.
26 J. Liu, *et al.*, Perovskite/silicon tandem solar cells with bilayer interface passivation, *Nature*, 2024, **635**, 596–603, DOI: **10.1038/s41586-024-07997-7**.
27 P. Wu, S. Wang, X. Li and F. Zhang, Beyond efficiency fever: Preventing lead leakage for perovskite solar cells, *Matter*, 2022, **5**, 1137–1161, DOI: **10.1016/j.matt.2022.02.012**.
28 S. K. Podapangi, *et al.*, Green solvents, materials, and lead-free semiconductors for sustainable fabrication of perovskite solar cells, *RSC Adv.*, 2023, **13**, 18165–18206, DOI: **10.1039/d3ra01692g**.
29 A. S. R. Bati, *et al.*, Next-generation applications for integrated perovskite solar cells, *Commun. Mater.*, 2023, **4**, 2, DOI: **10.1038/s43246-022-00325-4**.
30 I. Spanopoulos, W. Ke and M. G. Kanatzidis, In quest of environmentally stable perovskite solar cells: a perspective, *Helv. Chim. Acta*, 2020, **104**, e2000173, DOI: **10.1002/hlca.202000173**.
31 T. Baumeler, *et al.*, Champion device architectures for low-cost and stable single-junction perovskite solar cells, *ACS Mater. Lett.*, 2023, **5**, 2408–2421, DOI: **10.1021/acsmaterialslett.3c00337**.
32 M. I. Asghar, J. Zhang, H. Wang and P. D. Lund, Device stability of perovskite solar cells – A review, *Renewable Sustainable Energy Rev.*, 2017, **77**, 131–146, DOI: **10.1016/j.rser.2017.04.003**.
33 K. Deng and L. Li, Optical design in perovskite solar cells, *Small Methods*, 2019, **4**, 1900150, DOI: **10.1002/smtd.201900150**.
34 Y. Rong, *et al.*, Challenges for commercializing perovskite solar cells, *Science*, 2018, **361**, eaat8235, DOI: **10.1126/science.aat8235**.
35 L. Liang, Y. Cai, X. Li, M. K. Nazeeruddin and P. Gao, All that glitters is not gold: Recent progress of alternative counter electrodes for perovskite solar cells, *Nano Energy*, 2018, **52**, 211–238, DOI: **10.1016/j.nanoen.2018.07.049**.
36 T. Xu, L. Chen, Z. Guo and T. Ma, Strategic improvement of the long-term stability of perovskite materials and perovskite solar cells, *Phys. Chem. Chem. Phys.*, 2016, **18**, 27026–27050, DOI: **10.1039/c6cp04553g**.
37 R. He, X. Huang, M. Chee, F. Hao and P. Dong, Carbon-based perovskite solar cells: From single-junction to modules, *Carbon Energy*, 2019, **1**, 109–123, DOI: **10.1002/cey2.11**.

38 Z. Wu, T. Song and B. Sun, Carbon-based materials used for perovskite solar cells, *ChemNanoMat*, 2016, **3**, 75–88, DOI: **10.1002/cnma.201600312**.

39 M. Hadadian, J.-H. Smått and J.-P. Correa-Baena, The role of carbon-based materials in enhancing the stability of perovskite solar cells, *Energy Environ. Sci.*, 2020, **13**, 1377–1407, DOI: **10.1039/c9ee04030g**.

40 D. Pourjafari, *et al.*, Functional materials for fabrication of carbon-based perovskite solar cells: ink formulation and its effect on solar cell performance, *Materials*, 2023, **16**, 3917, DOI: **10.3390/ma16113917**.

41 S. Pandey, *et al.*, Recent advances in carbon-based materials for high-performance perovskite solar cells: gaps, challenges and fulfillment, *Nanoscale Adv.*, 2023, **5**, 1492–1526, DOI: **10.1039/d3na00005b**.

42 P. Mariani, *et al.*, Low-temperature graphene-based paste for large-area carbon perovskite solar cells, *ACS Appl. Mater. Interfaces*, 2021, **13**, 22368–22380, DOI: **10.1021/acsami.1c02626**.

43 D. Bogachuk, *et al.*, Low-temperature carbon-based electrodes in perovskite solar cells, *Energy Environ. Sci.*, 2020, **13**, 3880–3916, DOI: **10.1039/d0ee02175j**.

44 L. Fagiolari and F. Bella, Carbon-based materials for stable, cheaper and large-scale processable perovskite solar cells, *Energy Environ. Sci.*, 2019, **12**, 3437–3472, DOI: **10.1039/c9ee02115a**.

45 E. C. Kohlrausch, *et al.*, Advances in Carbon Materials Applied to Carbon-Based Perovskite Solar Cells, *Energy Technol.*, 2023, **11**, 2200676, DOI: **10.1002/ente.202200676**.

46 Y. Yu, M. T. Hoang, Y. Yang and H. Wang, Critical assessment of carbon pastes for carbon electrode-based perovskite solar cells, *Carbon*, 2023, **205**, 270–293, DOI: **10.1016/j.carbon.2023.01.046**.

47 M. Bidikoudi and E. Stathatos, Carbon electrodes: The rising star for PSC commercialization, *Electronics*, 2023, **12**, 992, DOI: **10.3390/electronics12040992**.

48 M. Wu, M. Sun, H. Zhou, J. Y. Ma and T. Ma, Carbon counter electrodes in dye-sensitized and perovskite solar cells, *Adv. Funct. Mater.*, 2019, **30**, 1906451, DOI: **10.1002/adfm.201906451**.

49 D. Beynon, *et al.*, All-Printed Roll-to-Roll Perovskite Photovoltaics Enabled by Solution-Processed Carbon Electrode, *Adv. Mater.*, 2023, **35**, e2208561, DOI: **10.1002/adma.202208561**.

50 H. C. Weerasinghe, *et al.*, The first demonstration of entirely roll-to-roll fabricated perovskite solar cell modules under ambient room conditions, *Nat. Commun.*, 2024, **15**, 1656, DOI: **10.1038/s41467-024-46016-1**.

51 E. Parvazian and T. Watson, The roll-to-roll revolution to tackle the industrial leap for perovskite solar cells, *Nat. Commun.*, 2024, **15**, 3983, DOI: **10.1038/s41467-024-48518-4**.

52 S. K. Yadav, Hydrophobic compressed carbon/graphite based long-term stable perovskite solar cells, *Mater. Chem. Phys.*, 2021, **268**, 124709, DOI: **10.1016/j.matchemphys.2021.124709**.

53 G. Grancini, *et al.*, One-Year stable perovskite solar cells by 2D/3D interface engineering, *Nat. Commun.*, 2017, **8**, 15684, DOI: **10.1038/ncomms15684**.

54 W. Yu, *et al.*, Carbon-based perovskite solar cells with electron and hole-transporting/-blocking layers, *Mater. Futures*, 2023, **2**, 022101, DOI: **10.1088/2752-5724/acbbc2**.

55 Z. Ku, Y. Rong, M. Xu, T. Liu and H. Han, Full printable processed mesoscopic CH3NH3PbI3/TiO2 heterojunction solar cells with carbon counter electrode, *Sci. Rep.*, 2013, **3**, 3132, DOI: **10.1038/srep03132**.

56 H. Han, U. Bach, Y.-B. Cheng, R. A. Caruso and C. MacRae, A design for monolithic all-solid-state dye-sensitized solar cells with a platinized carbon counterelectrode, *Appl. Phys. Lett.*, 2009, **94**, 103102, DOI: **10.1063/1.3086895**.

57 H. Chen, *et al.*, Solvent engineering boosts the efficiency of paintable carbon-based perovskite solar cells to beyond 14%, *Adv. Energy Mater.*, 2016, **6**, 1502087, DOI: **10.1002/aenm.201502087**.

58 I. Jeon, *et al.*, Perovskite solar cells using carbon nanotubes both as cathode and as anode, *J. Phys. Chem. C*, 2017, **121**, 25743–25749, DOI: **10.1021/acs.jpcc.7b10334**.

59 H. Zhang, *et al.*, SrCl(2) derived perovskite facilitating a high efficiency of 16% in hole-conductor-free fully printable mesoscopic perovskite solar cells, *Adv. Mater.*, 2017, **29**, 1606608, DOI: **10.1002/adma.201606608**.

60 J. Liu, *et al.*, Electron injection and defect passivation for high-efficiency mesoporous perovskite solar cells, *Science*, 2024, **383**, 1198–1204, DOI: **10.1126/science.adk9089**.

61 F. Meng, D. Wang, J. Chang, J. Li and G. Wang, Application of Carbon Materials in Conductive Electrodes for Perovskite Solar Cells, *Sol. RRL*, 2024, **8**, 2301030, DOI: **10.1002/solr.202301030**.

62 S. Rahemi Ardekani, *et al.*, A comprehensive review on ultrasonic spray pyrolysis technique: Mechanism, main parameters and applications in condensed matter, *J. Anal. Appl. Pyrolysis*, 2019, **141**, 104631, DOI: **10.1016/j.jaap.2019.104631**.

63 L. Hu, J. Song, X. Yin, Z. Su and Z. Li, Research Progress on Polymer Solar Cells Based on PEDOT:PSS Electrodes, *Polymers*, 2020, **12**, 145, DOI: **10.3390/polym12010145**.

64 L. Biessmann, *et al.*, Monitoring the Swelling Behavior of PEDOT:PSS Electrodes under High Humidity Conditions, *ACS Appl. Mater. Interfaces*, 2018, **10**, 9865–9872, DOI: **10.1021/acsami.8b00446**.

65 S.-Y. Lien, *et al.*, Improving Optoelectrical Properties of PEDOT: PSS by Organic Additive and Acid Treatment, *Crystals*, 2022, **12**, 537, DOI: **10.3390/cryst12040537**.

66 Z. Liu, S. P. Lau and F. Yan, Functionalized graphene and other two-dimensional materials for photovoltaic devices: device design and processing, *Chem. Soc. Rev.*, 2015, **44**, 5638–5679, DOI: **10.1039/c4cs00455h**.

67 Z. Liu, J. Li and F. Yan, Package-free flexible organic solar cells with graphene top electrodes, *Adv. Mater.*, 2013, **25**, 4296–4301, DOI: **10.1002/adma.201205337**.

68 J. Du, S. Pei, L. Ma and H. M. Cheng, 25th anniversary article: carbon nanotube- and graphene-based transparent

conductive films for optoelectronic devices, *Adv. Mater.*, 2014, **26**, 1958–1991, DOI: 10.1002/adma.201304135.

69 M. B. Lee, C. T. Lee, G. R. Mong, W. W. F. Chong and S. M. Sanip, A bibliometric analysis on the development trend of graphene-based transparent conductive electrodes (2009–2022), *Mater. Today Sustain.*, 2024, **25**, 100650, DOI: 10.1016/j.mtsust.2023.100650.

70 N. Ueoka, A. S. Hidayat, H. Oshima, Y. Hijikata and Y. Matsuo, Facile Doping of 2,2,2-Trifluoroethanol to Single-Walled Carbon Nanotubes Electrodes for Durable Perovskite Solar Cells, *Photochem*, 2024, **4**, 319–333, DOI: 10.3390/photochem4030019.

71 V. H. Nguyen, *et al.*, Advances in Flexible Metallic Transparent Electrodes, *Small*, 2022, **18**, e2106006, DOI: 10.1002/smll.202106006.

72 H. Chen and S. Yang, Stabilizing and scaling up carbon-based perovskite solar cells, *J. Mater. Res.*, 2017, **32**, 3011–3020, DOI: 10.1557/jmr.2017.294.

73 H. Chen and S. Yang, Carbon-based perovskite solar cells without hole transport materials: The front runner to the market?, *Adv. Mater.*, 2017, **29**, 1603994, DOI: 10.1002/adma.201603994.

74 C. Liu, Y. B. Cheng and Z. Ge, Understanding of perovskite crystal growth and film formation in scalable deposition processes, *Chem. Soc. Rev.*, 2020, **49**, 1653–1687, DOI: 10.1039/c9cs00711c.

75 Z. Saki, M. M. Byranvand, N. Taghavinia, M. Kedia and M. Saliba, Solution-processed perovskite thin-films: the journey from lab- to large-scale solar cells, *Energy Environ. Sci.*, 2021, **14**, 5690–5722, DOI: 10.1039/D1EE02018H.

76 A. Agresti, F. Di Giacomo, S. Pescetelli and A. Di Carlo, Scalable deposition techniques for large-area perovskite photovoltaic technology: A multi-perspective review, *Nano Energy*, 2024, **122**, 109317, DOI: 10.1016/j.nanoen.2024.109317.

77 A. Zhu, *et al.*, Playdough-like carbon electrode: A promising strategy for high efficiency perovskite solar cells and modules, *eScience*, 2024, **4**, 100221, DOI: 10.1016/j.esci.2023.100221.

78 Y. Yang, *et al.*, High performance carbon-based planar perovskite solar cells by hot-pressing approach, *Sol. Energy Mater. Sol. Cells*, 2020, **210**, 110517, DOI: 10.1016/j.solmat.2020.110517.

79 H. Zhang, *et al.*, Self-adhesive macroporous carbon electrodes for efficient and stable perovskite solar cells, *Adv. Funct. Mater.*, 2018, **28**, 1802985, DOI: 10.1002/adfm.201802985.

80 L. J. Sutherland, *et al.*, A high-pressure isostatic lamination technique to fabricate versatile carbon electrode-based perovskite solar cells, *Commun. Mater.*, 2024, **5**, 90, DOI: 10.1038/s43246-024-00530-3.

81 Y. Zhang, *et al.*, Enhancing the performance and stability of carbon-based perovskite solar cells by the cold isostatic pressing method, *RSC Adv.*, 2017, **7**, 48958–48961, DOI: 10.1039/C7RA07579K.

82 Q. Duan, *et al.*, Vacuum-Assisted Laminating Preparation for Carbon Film Electrode in Perovskite Solar Cells, *Energy Technol.*, 2022, **10**, 2200320, DOI: 10.1002/ente.202200320.

83 G. Huang, *et al.*, Achieving over 20% Efficiency in Laminated HTM-Free Carbon Electrode Perovskite Solar Cells through *In Situ* Interface Reconstruction, *Angew. Chem., Int. Ed.*, 2024, e202420687, DOI: 10.1002/anie.202420687.

84 H. Wei, *et al.*, Free-standing flexible carbon electrode for highly efficient hole-conductor-free perovskite solar cells, *Carbon*, 2015, **93**, 861–868, DOI: 10.1016/j.carbon.2015.05.042.

85 E. Baghestani, *et al.*, A conductive adhesive ink for carbon-laminated perovskite solar cells with enhanced stability and high efficiency, *Sol. Energy*, 2023, **266**, 112165, DOI: 10.1016/j.solener.2023.112165.

86 J. Kim, *et al.*, Self-Encapsulable Carbon Electrode for Efficient and Stable Perovskite Solar Cells, *Sol. RRL*, 2023, **7**, 2300559, DOI: 10.1002/solr.202300559.

87 Y. Gou, *et al.*, Work Function Tuning of Carbon Electrode to Boost the Charge Extraction in Hole Transport Layer-Free Perovskite Solar Cells, *Small*, 2024, **20**, e2403342, DOI: 10.1002/smll.202403342.

88 J. Wang, *et al.*, Tuning an Electrode Work Function Using Organometallic Complexes in Inverted Perovskite Solar Cells, *J. Am. Chem. Soc.*, 2021, **143**, 7759–7768, DOI: 10.1021/jacs.1c02118.

89 Y. Shi, *et al.*, Work Function Engineering of Graphene Electrode *via* Chemical Doping, *ACS Nano*, 2010, **4**, 2689–2694.

90 S. Liu, V. P. Biju, Y. Qi, W. Chen and Z. Liu, Recent progress in the development of high-efficiency inverted perovskite solar cells, *NPG Asia Mater.*, 2023, **15**, 27, DOI: 10.1038/s41427-023-00474-z.

91 S. Pescetelli, *et al.*, Integration of two-dimensional materials-based perovskite solar panels into a stand-alone solar farm, *Nat. Energy*, 2022, **7**, 597–607, DOI: 10.1038/s41560-022-01035-4.

92 M. Stefanelli, L. Vesce and A. Di Carlo, Upscaling of Carbon-Based Perovskite Solar Module, *Nanomaterials*, 2023, **13**, 313, DOI: 10.3390/nano13020313.

93 S. Razza, S. Pescetelli, A. Agresti and A. Di Carlo, Laser processing optimization for large-area perovskite solar modules, *Energies*, 2021, **14**, 1069, DOI: 10.3390/en14041069.

94 S. H. Reddy, F. Di Giacomo and A. Di Carlo, Low-Temperature-Processed Stable Perovskite Solar Cells and Modules: A Comprehensive Review, *Adv. Energy Mater.*, 2022, **12**, 2103534, DOI: 10.1002/aenm.202103534.

95 F. Di Giacomo, L. A. Castriotta, F. Matteocci and A. Di Carlo, Beyond 99.5% Geometrical Fill Factor in Perovskite Solar Minimodules with Advanced Laser Structuring, *Adv. Energy Mater.*, 2024, **14**, 2400115, DOI: 10.1002/aenm.202400115.

96 A. Agresti, *et al.*, Two-dimensional material interface engineering for efficient perovskite large-area modules, *ACS Energy Lett.*, 2019, **4**, 1862–1871, DOI: 10.1021/acsenergylett.9b01151.

97 F. Di Giacomo, *et al.*, Upscaling Inverted Perovskite Solar Cells: Optimization of Laser Scribing for Highly Efficient Mini-Modules, *Micromachines*, 2020, **11**, 1127, DOI: 10.3390/mi11121127.

98 S. Pitchaiya, N. Eswaramoorthy, V. Madurai Ramakrishnan, M. Natarajan and D. Velauthapillai, Bio-inspired graphitic carbon-based large-area (10 x 10 cm(2)) perovskite solar cells: stability assessments under indoor, outdoor, and water-soaked conditions, *ACS Appl. Mater. Interfaces*, 2022, **14**, 43050–43066, DOI: 10.1021/acsami.2c02463.

99 D. Selvakumar, G. Murugadoss, A. Alsalme, A. M. Alkathiri and R. Jayavel, Heteroatom doped reduced graphene oxide paper for large area perovskite solar cells, *Sol. Energy*, 2018, **163**, 564–569, DOI: 10.1016/j.solener.2018.01.084.

100 N. Srisamran, *et al.*, Enhanced performance and stability of fully printed perovskite solar cells and modules by ternary additives under high humidity, *Energy Fuels*, 2023, **37**, 6049–6061, DOI: 10.1021/acs.energyfuels.2c03641.

101 D. Li, *et al.*, Series resistance modulation for large-area fully printable mesoscopic perovskite solar cells, *Sol. RRL*, 2021, **6**, 2100554, DOI: 10.1002/solr.202100554.

102 C. Zhang, *et al.*, Efficient stable graphene-based perovskite solar cells with high flexibility in device assembling *via* modular architecture design, *Energy Environ. Sci.*, 2019, **12**, 3585–3594, DOI: 10.1039/c9ee02391g.

103 Y. Ren, *et al.*, Long-chain gemini surfactant-assisted blade coating enables large-area carbon-based perovskite solar modules with record performance, *Nano-Micro Lett.*, 2023, **15**, 182, DOI: 10.1007/s40820-023-01155-w.

104 M. Li, *et al.*, Nickel-doped graphite and fusible alloy bilayer back electrode for vacuum-free perovskite solar cells, *ACS Energy Lett.*, 2023, **8**, 2940–2945, DOI: 10.1021/acsenergylett.3c00852.

105 L. Luo, *et al.*, Stabilization of 3D/2D perovskite heterostructures *via* inhibition of ion diffusion by cross-linked polymers for solar cells with improved performance, *Nat. Energy*, 2023, **8**, 294–303, DOI: 10.10138/s41560-023-01205-y.

106 D. B. Ritzer, *et al.*, Upscaling of perovskite solar modules: The synergy of fully evaporated layer fabrication and all-laser-scribed interconnections, *Prog. Photovolt.: Res. Appl.*, 2022, **30**, 360–373, DOI: 10.1002/pip.3489.

107 C. Chen, *et al.*, Perovskite solar cells based on screen-printed thin films, *Nature*, 2022, **612**, 266–271, DOI: 10.1038/s41586-022-05346-0.

108 C. Chen, *et al.*, Screen-Printing Technology for Scale Manufacturing of Perovskite Solar Cells, *Adv. Sci.*, 2023, **10**, e2303992, DOI: 10.1002/advs.202303992.

109 B. Wilkinson, N. L. Chang, M. A. Green and A. W. Ho-Baillie, Scaling limits to large area perovskite solar cell efficiency, *Prog. Photovolt.: Res. Appl.*, 2018, **26**, 659–674, DOI: 10.1002/pip.3035.

110 X. Jiang, *et al.*, Designing large-area single-crystal perovskite solar cells, *ACS Energy Lett.*, 2020, **5**, 1797–1803, DOI: 10.1021/acsenergylett.0c00436.

111 J. Weber and T. Roessler, How to assess the electrical quality of solar cell interconnection in shingle solar modules, *Prog. Photovolt.: Res. Appl.*, 2023, **31**, 949–959, DOI: 10.1002/pip.3699.

112 J. M. C. da Silva Filho, *et al.*, Investigation of the stability of metallic grids for large-area perovskite solar cells, *Sol. Energy Mater. Sol. Cells*, 2024, **276**, 113043, DOI: 10.1016/j.solmat.2024.113043.

113 S. A. Awuku, A. Bennadji, F. Muhammad-Sukki and N. Sellami, Myth or gold? The power of aesthetics in the adoption of building integrated photovoltaics (BIPVs), *Energy Nexus*, 2021, **4**, 100021, DOI: 10.1016/j.nexus.2021.100021.

114 L. Cai, *et al.*, Large area perovskite solar cell module, *J. Semicond.*, 2017, **38**, 014006, DOI: 10.1088/1674-4926/38/1/014006.

115 Y. Hu, *et al.*, Stable large-area (10 × 10 cm2) printable mesoscopic perovskite module exceeding 10% efficiency, *Sol. RRL*, 2017, **1**, 1600019, DOI: 10.1002/solr.201600019.

116 A. Priyadarshi, *et al.*, A large area (70 cm^2) monolithic perovskite solar module with a high efficiency and stability, *Energy Environ. Sci.*, 2016, **9**, 3687–3692, DOI: 10.1039/c6ee02693a.

117 F. De Rossi, *et al.*, All printable perovskite solar modules with 198 cm2 active area and over 6% efficiency, *Adv. Mater. Technol.*, 2018, **3**, 1800156, DOI: 10.1002/admt.201800156.

118 https://www.perovskite-info.com/.

119 J. Liu, T. Ye, D. Yu, S. F. Liu and D. Yang, Recoverable flexible perovskite solar cells for next-generation portable power sources, *Angew. Chem., Int. Ed. Engl.*, 2023, **62**, e202307225, DOI: 10.1002/anie.202307225.

120 J. H. Heo, D. H. Shin, M. L. Lee, M. G. Kang and S. H. Im, Efficient organic-inorganic hybrid flexible perovskite solar cells prepared by lamination of polytriarylamine/CH(3)NH(3)PbI(3)/anodized Ti metal substrate and graphene/PDMS transparent electrode substrate, *ACS Appl. Mater. Interfaces*, 2018, **10**, 31413–31421, DOI: 10.1021/acsami.8b11411.

121 Z. Zhang, *et al.*, Accelerated sequential deposition reaction *via* crystal orientation engineering for low-temperature, high-efficiency carbon-electrode CsPbBr3 solar cells, *Energy Environ. Mater.*, 2023, **7**, e12524, DOI: 10.1002/eem2.12524.

122 F. Deng, *et al.*, Highly Efficient (>13%) and Robust Flexible Perovskite Solar Cells Using an Ultrasimple All-Carbon-Electrode Configuration, *ACS Appl. Mater. Interfaces*, 2023, **15**, 46054–46063, DOI: 10.1021/acsami.3c09761.

123 W. Passatorntaschakorn, *et al.*, A novel carbon electrode for up-scaling flexible perovskite solar cells, *Appl. Mater. Today*, 2023, **34**, 101895, DOI: 10.1016/j.apmt.2023.101895.

124 C. Peng, *et al.*, Scalable, efficient and flexible perovskite solar cells with carbon film based electrode, *Sol. Energy Mater. Sol. Cells*, 2021, **230**, 111226, DOI: 10.1016/j.solmat.2021.111226.

125 V. Babu, *et al.*, Improved stability of inverted and flexible perovskite solar cells with carbon electrode, *ACS Appl. Energy Mater.*, 2020, **3**, 5126–5134, DOI: 10.1021/acsaem.0c00702.

126 J. Yoon, *et al.*, Superflexible, high-efficiency perovskite solar cells utilizing graphene electrodes: towards future foldable power sources, *Energy Environ. Sci.*, 2017, **10**, 337–345, DOI: 10.1039/c6ee02650h.

127 G. Lee, *et al.*, Ultra-flexible perovskite solar cells with crumpling durability: toward a wearable power source, *Energy Environ. Sci.*, 2019, **12**, 3182–3191, DOI: 10.1039/c9ee01944h.

128 M.-c. Kim, *et al.*, Degradation of CH3NH3PbI3 perovskite materials by localized charges and its polarity dependency, *J. Mater. Chem. A*, 2019, **7**, 12075–12085, DOI: 10.1039/c9ta03180d.

129 M.-c. Kim, *et al.*, Imaging Real-Time Amorphization of Hybrid Perovskite Solar Cells under Electrical Biasing, *ACS Energy Lett.*, 2021, **6**, 3530–3537, DOI: 10.1021/acsenergylett.1c01707.

130 A. A. Sutanto, *et al.*, Dynamical evolution of the 2D/3D interface: a hidden driver behind perovskite solar cell instability, *J. Mater. Chem. A*, 2020, **8**, 2343–2348, DOI: 10.1039/c9ta12489f.

131 A. A. Sutanto, *et al.*, *In Situ* Analysis Reveals the Role of 2D Perovskite in Preventing Thermal-Induced Degradation in 2D/3D Perovskite Interfaces, *Nano Lett.*, 2020, **20**, 3992–3998, DOI: 10.1021/acs.nanolett.0c01271.

132 K. Lee, *et al.*, A highly stable and efficient carbon electrode-based perovskite solar cell achieved *via* interfacial growth of 2D PEA2PbI4 perovskite, *J. Mater. Chem. A*, 2018, **6**, 24560–24568, DOI: 10.1039/c8ta09433k.

133 P. Kartikay, *et al.*, Visualizing interfacial defect passivation in carbon-based perovskite solar cells, *Int. J. Energy Res.*, 2022, **46**, 22704–22716, DOI: 10.1002/er.8573.

134 G. Grancini *et al.*, Ultra-stable 2D/3D hybrid perovskite photovoltaic module, *arXiv*, 2016, preprint, arXiv:1609.09846, DOI: 10.48550/arXiv.1609.09846.

135 J. Wu, *et al.*, Highly orientational order perovskite induced by in situ-generated 1D perovskitoid for efficient and stable printable photovoltaics, *Small*, 2022, **18**, e2200130, DOI: 10.1002/smll.202200130.

136 P. Kartikay, A. Paul, A. Yella and S. Mallick, Cation exchange enabled improved perovskite infiltration in triple-mesoscopic carbon perovskite solar cells, *Mater. Chem. Phys.*, 2023, **307**, 128181, DOI: 10.1016/j.matchemphys.2023.128181.

137 L. T. D. Thach, *et al.*, Using solvent vapor annealing for the enhancement of the stability and efficiency of monolithic hole-conductor-free perovskite solar cells, *Commun. phys.*, 2020, **30**, 133, DOI: 10.15625/0868-3166/30/2/14657.

138 P. Li, *et al.*, Phase pure 2D perovskite for high-performance 2D-3D heterostructured perovskite solar cells, *Adv. Mater.*, 2018, **30**, e1805323, DOI: 10.1002/adma.201805323.

139 F. Meng, *et al.*, Ultra-low-cost coal-based carbon electrodes with seamless interfacial contact for effective sandwich-structured perovskite solar cells, *Carbon*, 2019, **145**, 290–296, DOI: 10.1016/j.carbon.2019.01.047.

140 L. Gao, *et al.*, Several economical and eco-friendly bio-carbon electrodes for highly efficient perovskite solar cells, *Carbon*, 2020, **162**, 267–272, DOI: 10.1016/j.carbon.2020.02.049.

141 H. Liu, *et al.*, Improving the performance and stability of large-area carbon-based perovskite solar cells using N, O co-doped biomass porous carbon, *J. Alloys Compd.*, 2022, **912**, 165123, DOI: 10.1016/j.jallcom.2022.165123.

142 R. Chen, *et al.*, Carbon-based HTL-free modular perovskite solar cells with improved contact at perovskite/carbon interfaces, *J. Mater. Chem. C*, 2020, **8**, 9262–9270, DOI: 10.1039/d0tc02226h.

143 R. Chen, *et al.*, Low-temperature sprayed carbon electrode in modular HTL-free perovskite solar cells: a comparative study on the choice of carbon sources, *J. Mater. Chem. C*, 2021, **9**, 3546–3554, DOI: 10.1039/d0tc05528j.

144 S. Sajid, *et al.*, NiO@carbon spheres: A promising composite electrode for scalable fabrication of planar perovskite solar cells at low cost, *Nano Energy*, 2019, **55**, 470–476, DOI: 10.1016/j.nanoen.2018.11.004.

145 J. Han, *et al.*, High efficient large-area perovskite solar cells based on paintable carbon electrode with NiO nanocrystal-carbon intermediate layer, *Chem. Lett.*, 2019, **48**, 734–737, DOI: 10.1246/cl.190210.

146 B. Yu, *et al.*, Regulating three-layer full carbon electrodes to enhance the cell performance of CsPbI(3) perovskite solar cells, *Nat. Commun.*, 2025, **16**, 3328, DOI: 10.1038/s41467-025-58672-y.

147 Y. Yang, *et al.*, An ultrathin ferroelectric perovskite oxide layer for high-performance hole transport material free carbon based halide perovskite solar cells, *Adv. Funct. Mater.*, 2018, **29**, 1806506, DOI: 10.1002/adfm.201806506.

148 L. Zhang, *et al.*, Inkjet-printing controlled phase evolution boosts the efficiency of hole transport material free and carbon-based CsPbBr3 perovskite solar cells exceeding 9%, *Energy Environ. Mater.*, 2023, **7**, e12543, DOI: 10.1002/eem2.12543.

149 J. Han, *et al.*, An excellent modifier: carbon quantum dots for highly efficient carbon-electrode-based methylammonium lead iodide solar cells, *Sol. RRL*, 2019, **3**, 1900146, DOI: 10.1002/solr.201900146.

150 Q. Sun, *et al.*, Efficient and stable large-area perovskite solar cells with inorganic perovskite/carbon quantum dot-graded heterojunction, *Research*, 2021, 9845067, DOI: 10.34133/2021/9845067.

151 R. Guo, *et al.*, Effective defect passivation with a designer ionic molecule for high-efficiency vapour-deposited inorganic phase-pure CsPbBr3 perovskite solar cells, *J. Mater. Chem. A*, 2023, **11**, 408–418, DOI: 10.1039/d2ta06092b.

152 H. Xiao, *et al.*, Highly efficient and air-stable inorganic perovskite solar cells enabled by polylactic acid modification, *Adv. Energy Mater.*, 2023, **13**, 2300738, DOI: 10.1002/aenm.202300738.

153 Y. Xu, *et al.*, Mxene regulates the stress of perovskite and improves interfacecontact for high-efficiency carbon-based all-inorganic solar cells, *Chem. Eng. J.*, 2023, **461**, 141895, DOI: 10.1016/j.cej.2023.141895.

154 J. Ryu, *et al.*, Paintable carbon-based perovskite solar cells with engineered perovskite/carbon interface using carbon nanotubes dripping method, *Small*, 2017, **13**, 1701225, DOI: 10.1002/smll.201701225.

155 E. Calabro, *et al.*, Easy strategy to enhance thermal stability of planar PSCs by perovskite defect passivation and low-temperature carbon-based electrode, *ACS Appl. Mater. Interfaces*, 2020, **12**, 32536–32547, DOI: 10.1021/acsami.0c05878.

156 T. Liu, *et al.*, Interfacial post-treatment for enhancing the performance of printable carbon-based perovskite solar cells, *Sol. RRL*, 2019, **4**, 1900278, DOI: 10.1002/solr.201900278.

157 S. Iqbal, *et al.*, Fully printed HTL-free MAPbI3 perovskite solar cells with carbon electrodes, *Coatings*, 2023, **13**, 1338, DOI: 10.3390/coatings13081338.

158 H. Chen, *et al.*, Solvent engineering boosts the efficiency of paintable carbon-based perovskite solar cells to beyond 14%, *Adv. Energy Mater.*, 2016, **6**, 1502087, DOI: 10.1002/aenm.201502087.

159 S. M. P. Meroni, *et al.*, Homogeneous and highly controlled deposition of low viscosity inks and application on fully printable perovskite solar cells, *Sci. Technol. Adv. Mater.*, 2017, **19**, 1–9, DOI: 10.1080/14686996.2017.1406777.

160 D. Raptis, *et al.*, Scalable screen-printed TiO_2 compact layers for fully printable carbon-based perovskite solar cells, *Solar*, 2022, **2**, 293–304, DOI: 10.3390/solar2020016.

161 C. Worsley, *et al.*, Green solvent engineering for enhanced performance and reproducibility in printed carbon-based mesoscopic perovskite solar cells and modules, *Mater. Adv.*, 2022, **3**, 1125–1138, DOI: 10.1039/d1ma00975c.

162 G. Wang, *et al.*, High-performance carbon electrode-based CsPbI(2)Br inorganic perovskite solar cell based on poly(3-hexylthiophene)-carbon nanotubes composite hole-transporting layer, *J. Colloid Interface Sci.*, 2019, **555**, 180–186, DOI: 10.1016/j.jcis.2019.07.084.

163 H. Su, *et al.*, Carbon film electrode based square-centimeter scale planar perovskite solar cells exceeding 17% efficiency, *Mater. Sci. Semicond. Process.*, 2020, **107**, 104809, DOI: 10.1016/j.mssp.2019.104809.

164 P. Ruankham, N. Khambunkoed, P. Kanjanaboos, D. Wongratanaphisan and T. Sagawa, Improved reproducibility of carbon-based cesium/formamidinium perovskite solar cells *via* double antisolvent drippings in adduct approach, *Org. Electron.*, 2022, **100**, 106362, DOI: 10.1016/j.orgel.2021.106362.

165 M. Xu, *et al.*, Efficient triple-mesoscopic perovskite solar mini-modules fabricated with slot-die coating, *Nano Energy*, 2020, **74**, 104842, DOI: 10.1016/j.nanoen.2020.104842.

166 D. Raptis, *et al.*, Enhancing fully printable mesoscopic perovskite solar cell performance using integrated metallic grids to improve carbon electrode conductivity, *Curr. Appl. Phys.*, 2020, **20**, 619–627, DOI: 10.1016/j.cap.2020.02.009.

167 D. Bogachuk, *et al.*, Perovskite photovoltaic devices with carbon-based electrodes withstanding reverse-bias voltages up to −9 V and surpassing IEC 61215:2016 international standard, *Sol. RRL*, 2022, **6**, 2100527, DOI: 10.1002/solr.202100527.

168 C. Worsley, S.-J. Potts, D. Hughes, W. C. Tsoi and T. Watson, Age-induced excellence with green solvents: the impact of residual solvent and post-treatments in screen-printed carbon perovskite solar cells and modules, *Mater. Adv.*, 2024, **5**, 4354–4365, DOI: 10.1039/d4ma00136b.

169 E. Planes, *et al.*, Interface Effects on the Stability of Carbon-Electrode-Based Perovskite Solar Cells During Damp Heating, *Adv. Mater. Interfaces*, 2024, **11**, 2300849, DOI: 10.1002/admi.202300849.

170 K. S. Keremane, *et al.*, Improving the performance of carbon-based perovskite solar modules (70 cm^2) by incorporating cesium halide in mesoporous TiO2, *ACS Appl. Energy Mater.*, 2020, **4**, 249–258, DOI: 10.1021/acsaem.0c02213.

171 S. Li, *et al.*, Hole transport layer-free carbon-based perovskite solar cells with high-efficiency up to 17.49% in air: From-bottom-to-top perovskite interface modification, *Chem. Eng. J.*, 2023, **455**, 140727, DOI: 10.1016/j.cej.2022.140727.

172 F. Meng, *et al.*, Environmental risks and strategies for long-term stability of carbon-based perovskite solar cells, *Mater. Today Energy*, 2021, **19**, 100590, DOI: 10.1016/j.mtener.2020.100590.

173 Y. Tian, *et al.*, Organic bromide salts interface modification for high-efficiency perovskite solar cells with printed carbon electrode, *Energy Technol.*, 2023, **11**, 2300454, DOI: 10.1002/ente.202300454.

174 C. T. K. Mai, *et al.*, Super-Droplet-Repellent Carbon-Based Printable Perovskite Solar Cells, *Adv. Sci.*, 2024, **11**, e2401016, DOI: 10.1002/advs.202401016.

175 B. Parida, *et al.*, Recent Developments in Upscalable Printing Techniques for Perovskite Solar Cells, *Adv. Sci.*, 2022, **9**, e2200308, DOI: 10.1002/advs.202200308.

176 A. Bashir, *et al.*, Spinel Co(3)O(4) nanomaterials for efficient and stable large area carbon-based printed perovskite solar cells, *Nanoscale*, 2018, **10**, 2341–2350, DOI: 10.1039/c7nr08289d.

177 A. Bashir, *et al.*, Cu-doped nickel oxide interface layer with nanoscale thickness for efficient and highly stable printable carbon-based perovskite solar cell, *Sol. Energy*, 2019, **182**, 225–236, DOI: 10.1016/j.solener.2019.02.056.

178 F. Han, *et al.*, Hyperstable perovskite solar cells without ion migration and metal diffusion based on ZnS segregated Cubic ZnTiO3 electron transport layers, *Sol. RRL*, 2021, **5**, 2000654, DOI: 10.1002/solr.202000654.

179 L. Vesce, M. Stefanelli, H. Nikbakht and A. Di Carlo, Process engineering for low-temperature carbon-based perovskite solar modules, *Eng. Proc.*, 2023, **37**, 29, DOI: 10.3390/xxxx.

180 F. Yang, *et al.*, Low temperature processed fully printed efficient planar structure carbon electrode perovskite solar cells and modules, *Adv. Energy Mater.*, 2021, **11**, 2101219, DOI: 10.1002/aenm.202101219.

181 D. A. Chalkias, *et al.*, Suppression of coffee-ring effect in air-processed inkjet-printed perovskite layer toward the

fabrication of efficient large-sized all-printed photovoltaics: a perovskite precursor ink concentration regulation strategy, *Sol. RRL*, 2022, **6**, 2200196, DOI: **10.1002/solr.202200196**.

182 J. Zhou, J. Hou, X. Tao, X. Meng and S. Yang, Solution-processed electron transport layer of n-doped fullerene for efficient and stable all carbon based perovskite solar cells, *J. Mater. Chem. A*, 2019, **7**, 7710–7716, DOI: **10.1039/c9ta00118b**.

183 L. Lou, *et al.*, Controlling apparent coordinated solvent number in the perovskite intermediate phase film for developing large-area perovskite solar modules, *Energy Technol.*, 2019, **8**, 1900972, DOI: **10.1002/ente.201900972**.

184 S. S. Mali, *et al.*, Large area, waterproof, air stable and cost effective efficient perovskite solar cells through modified carbon hole extraction layer, *Mater. Today Chem.*, 2017, **4**, 53–63, DOI: **10.1016/j.mtchem.2016.12.003**.

185 M. V. Khenkin, *et al.*, Consensus statement for stability assessment and reporting for perovskite photovoltaics based on ISOS procedures, *Nat. Energy*, 2020, **5**, 35–49, DOI: **10.1038/s41560-019-0529-5**.

186 S. S. Mali, J. V. Patil and C. K. Hong, A 'Smart-Bottle' humidifier-assisted air-processed CuSCN inorganic hole extraction layer towards highly-efficient, large-area and thermally-stable perovskite solar cells, *J. Mater. Chem. A*, 2019, **7**, 10246–10255, DOI: **10.1039/c9ta01094g**.

187 F. Meng, *et al.*, Current progress in interfacial engineering of carbon-based perovskite solar cells, *J. Mater. Chem. A*, 2019, **7**, 8690–8699, DOI: **10.1039/c9ta01364d**.

188 S. Kim, *et al.*, Relationship between ion migration and interfacial degradation of CH(3)NH(3)PbI(3) perovskite solar cells under thermal conditions, *Sci. Rep.*, 2017, **7**, 1200, DOI: **10.1038/s41598-017-00866-6**.

189 T. A. Berhe, *et al.*, Organometal halide perovskite solar cells: degradation and stability, *Energy Environ. Sci.*, 2016, **9**, 323–356, DOI: **10.1039/c5ee02733k**.

190 L. Meng, J. You and Y. Yang, Addressing the stability issue of perovskite solar cells for commercial applications, *Nat. Commun.*, 2018, **9**, 5265, DOI: **10.1038/s41467-018-07255-1**.

191 G. Divitini, *et al.*, In situ observation of heat-induced degradation of perovskite solar cells, *Nat. Energy*, 2016, **1**, 1–6, DOI: **10.1038/nenergy.2015.12**.

192 B. Conings, *et al.*, Intrinsic thermal instability of methylammonium lead trihalide perovskite, *Adv. Energy Mater.*, 2015, **5**, 1500477, DOI: **10.1002/aenm.201500477**.

193 P. Mariani, *et al.*, Low-temperature strain-free encapsulation for perovskite solar cells and modules passing multifaceted accelerated ageing tests, *Nat. Commun.*, 2024, **15**, 4552, DOI: **10.1038/s41467-024-48877-y**.

194 G. Liu, *et al.*, Carbon Electrode Endows High-Efficiency Perovskite Photovoltaics Affordable, Fully Printable, and Durable, *Sol. RRL*, 2022, **6**, 2200258, DOI: **10.1002/solr.202200258**.

195 I. Albrahee, Y. Li and G. Xing, Carbon-based Perovskite Solar Cells: From Current Fabrication Methodologies to Their Future Commercialization at Low Cost, *Innov. Discov.*, 2025, **2**, 1, DOI: **10.53964/id.2025001**.

196 G. Li and H. Chen, Manufacturing Cost Analysis of Single-Junction Perovskite Solar Cells, *Sol. RRL*, 2024, **8**, 2400540, DOI: **10.1002/solr.202400540**.

197 N. Chang, *et al.*, A manufacturing cost estimation method with uncertainty analysis and its application to perovskite on glass photovoltaic modules, *Prog. Photovolt: Res. Appl.*, 2017, **25**, 309–405, DOI: **10.1002/pip.2871**.

198 M. Cai, *et al.*, Cost-performance analysis of perovskite solar modules, *Adv. Sci.*, 2017, **4**, 1600269.

199 Z. Song, *et al.*, A technoeconomic analysis of perovskite solar module manufacturing with low-cost materials and techniques, *Energy Environ. Sci.*, 2017, **10**, 1297–1305.

200 Z. Li, *et al.*, Cost analysis of perovskite tandem photovoltaics, *Joule*, 2018, **2**, 1559–1572.

201 S. Maniarasu, *et al.*, Recent advancement in metal cathode and hole-conductor-free perovskite solar cells for low-cost and high stability: A route towards commercialization, *Renewable Sustainable Energy Rev.*, 2018, **82**, 845–857, DOI: **10.1016/j.rser.2017.09.095**.

202 J. M. Choi, *et al.*, Overview and outlook on graphene and carbon nanotubes in perovskite photovoltaics from single-junction to tandem applications, *Adv. Funct. Mater.*, 2022, **32**, 2204594.

203 F. Lang, *et al.*, Perovskite Solar Cells with Large-Area CVD-Graphene for Tandem Solar Cells, *J. Phys. Chem. Lett.*, 2015, **6**, 2745–2750, DOI: **10.1021/acs.jpclett.5b01177**.

204 C. Lee, *et al.*, Carbon nanotube electrode-based perovskite–silicon tandem solar cells, *Sol. RRL*, 2020, **4**, 2000353.

205 P. Hang, *et al.*, Technoeconomically competitive four-terminal perovskite/graphene-silicon tandem solar cells with over 20% efficiency, *J. Energy Chem.*, 2021, **63**, 477–483.

206 E. Raza, *et al.*, A numerical approach to study the effect of bandgap and electron affinity in HTL-free perovskite solar cells and design of two-terminal silicon/perovskite tandem solar cell, *Mater. Today Commun.*, 2023, **37**, 107383, DOI: **10.1016/j.mtcomm.2023.107383**.

207 A. H. M. Fard and S. Matloub, Enhanced efficiency of carbon based all perovskite tandem solar cells *via* cubic plasmonic metallic nanoparticles with dielectric nano shells, *Sci. Rep.*, 2024, **14**, 26391, DOI: **10.1038/s41598-024-78165-0**.